The Nano-optimization of P- and E-type Semiconductor Films for Efficient Perovskite Photovoltaics

UNIVERSITY *of the* WESTERN CAPE

A Thesis submitted in fulfillment of the requirement for the degree of

Magister Scientiae in Nanoscience (Chemistry)

Department of Chemistry: SensorLab

University of the Western Cape

April 2022

By

Tamsen Orange

Supervisor: Dr. N. Ross

Co-supervisor: Prof. C. Arendse

Keywords

Perovskite Solar Cells

Power conversion efficiency

ITO glass substrate

Hole transporting material

Electron transporting material

Absorbing layer

J-V measurements

Abstract

Perovskite solar cells (PSCs) have gained a lot of attraction due to the multiple existing, inexpensive production methods, the flexibility of materials and structures that can be utilized, and the outstanding optoelectric properties, which include the high carrier diffusion length and strong absorption. Despite the multiple favourable characteristics, there are however unfavourable characteristics that are preventing the commercialization of these solar cells, namely, the scaling up of the spin-coating process, the stability of the cells, the toxicity because of the lead compounds used in the cells, and hysteresis in current-voltage (I-V) curves. Structural stability refers to the capability of the crystalline stage to resist degradation over a wide range of conditions, namely, moisture, pressure, and heat.

This project involves the determination of the most efficient, stable, and cost-effective solar cells using, $MAPbI_3$, $MAPbBr_3$, SnO_2, ZnO, and rGO. The materials underwent a spin-coating process to form the ETL, absorbing layer, and HTL before the device performance was measured using J-V measurements.

The synthesized materials, $MAPbI_3$, $MAPbBr_3$, SnO_2, ZnO, and rGO, were characterized using High-resolution scanning electron microscope (HRSEM), X-ray diffraction (XRD), Fourier transform infrared spectroscopy (FTIR), X-ray photoelectron spectroscopy (XPS), Ultraviolet-visible spectroscopy (UV-vis), Photoluminescence (PL), Cyclic voltammetry (CV), and Electrochemical impedance spectroscopy (EIS).

The HRSEM images, were used to investigate the layer of the materials on the ITO coated glass substrate and if the layers formed are uniform and free of irregularities. The crystalline structure and elemental composition of the materials were investigated using XRD, XPS, and FTIR.

The optical properties of the materials were investigated using UV-vis and PL, and the electronic properties were investigated using CV and EIS. The data obtained in UV-vis spectroscopy was used to calculate the bandgap of the materials, with values of 1.82, 2.30, 4.02, 3.40, and 1.67 eV for $MAPbI_3$, $MAPbBr_3$, SnO_2, ZnO, and rGO, respectively.

Lastly, J-V measurements were done to determine which PSC produced the highest efficiency. From the measurements, the PSC, SnO_2/$MAPbI_3$/Spiro, had the highest efficiency of 1.02%. The PSCs employing the ETM SnO_2 displayed efficiencies four times greater than their ZnO counterparts.

Declaration

I, hereby declare that "The nano-optimization of p- and e-type semiconductor films for efficient perovskite photovoltaics" is the result of my work that was done by me under the supervision of Dr. Natasha Ross and co-supervision of Prof. Christopher Arendse, and that it has not been previously submitted for any degree or examination in any other university or higher education; and that all sources and quotations have been indicated and acknowledged by complete references.

Tamsen Orange March 2020

Signed……. Date…11 April 2022……

Acknowledgments

I would like to thank our Lord Almighty, for granting me the wisdom, strength, resilience, and patience, to persevere despite the hardships. Thank you for blessing me with the opportunity to reach the goals I set for myself.

To my supervisor, Dr. Natasha Ross, I'd like to thank her for the endless support, guidance, time, and patience that she had invested in me to become a better researcher and for giving me the opportunity to be her student.

Furthermore, I would like to thank my co-supervisor, Prof. Christopher Arendse, for all the advice, suggestions, constructive criticism, and time given throughout this degree. These discussions with my supervisors led to improvements in the work done.

Thank you to my mother, Cornelia Orange, and my brother, Conry Orange for praying and supporting me daily. They were and are my pillars of strength, motivating and sharing words of encouragement with me.

I would like to thank my mentor, Kevin Tambwe, and friends from the chemistry department, Ashiqa Fakier, Jaymi January, and Kaylin Januarie, for helping and advising me whenever they had the opportunity to do so and helping me find my way back with words of encouragement and advise when things were not going as planned.

I would like to thank the Nanoscience Platform for the financial support throughout this degree and for the extension in their support which has helped me tremendously.

Lastly, I would like to thank the members of the SensorLab research group and the Physics Department for their help, support, and kindness throughout this degree.

List of Abbreviations

AM 1.5G	Air-mass 1.5 global analysis
ATR	Attenuated total reflection
CV	Cyclic Voltammetry
CVD	Chemical Vapour Deposition
EDS	Energy Dispersive Spectroscopy
EIS	Electrochemical Impedance Spectroscopy
ETL	Electron Transport Layer
ETM	Electron Transporting Material
EWT	Emitter wrap-through
FF	Fill Factor
FTIR	Fourier Transform Infrared Spectroscopy
FSP	Flame Spray Pyrolysis
HOMO	Highest occupied molecular orbital
HRSEM	High Resolution Scanning Electron Microscope
HTL	Hole Transporting Layer
HTM	Hole Transporting Material
Hz	Hertz
ICSD	Inorganic Crystal Structure Database
J-V	Current density-voltage curves
J_{SC}	Short circuit current
kW	Kilowatt
LUMO	Lowest occupied molecular orbital
PCE	Power Conversion Efficiency
PL	Photoluminescence
PSC	Perovskite Solar Cell
PV	Photovoltaic
QCM	Quartz Crystal Microbalance
R_{ct}	Charfe transfer resistance
R_s	Solution resistance
rGO	Reduced Graphene Oxide

Si p-n	Silicon positive-negative
T_g	Glass Transition Temperature
UV-vis	Ultraviolet-Visible Spectroscopy
V_{OC}	Open circuit potential
XPS	X-Ray Photoelectron Spectroscopy
XRD	X-Ray Diffraction

Table of Contents

List of Figures

List of Tables

CHAPTER ONE

Introduction

This chapter contains a brief introduction to solar cells, the introduction of perovskites in solar cells, their structure, and the principle of the photovoltaic effect. It also contains motivation and questions, aims and objectives of this investigation. The research approach is also detailed.

1.1. Background

The first organometal trihalide perovskite, was developed in 2009 when it was first introduced into dye-sensitized solar cells displaying a power conversion efficiency (PCE) of 3.81%.[1] After a decade, the PCE of perovskite solar cells (PSCs) has reached 25.5%, [2] which is attributed to a tremendous effort by the perovskite research community. Solar cells with high efficiencies require materials with superior light-absorbing properties. Within each cell structure, the material follows the photovoltaic effect whereby the material absorbs photons and generate free electrons [3]. A photocurrent arises from minority carriers generated by photo-excitation of the semiconductor absorber. An electric field present at the p-n junction separates the electrons and holes such that electrons flow to the n-doped layer and holes to the p-doped material, resulting in a net current flow as illustrated in Figure 1.1 below.

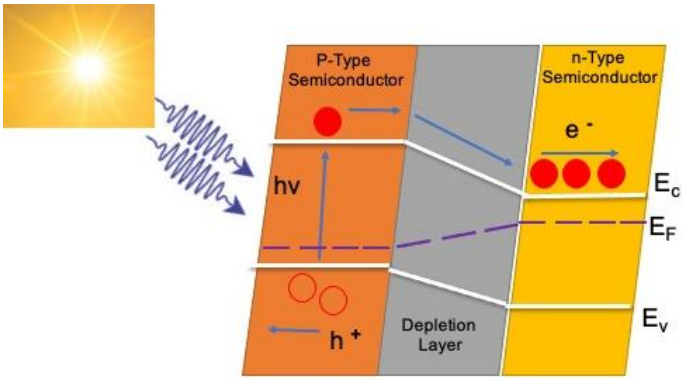

Figure 1.1: Schematic illustration of the photovoltaic effect. E_C, E_F and E_V are the energy levels of the conduction band minimum, the Fermi level and the valence band maximum, respectively.

Photovoltaics is achievable using various semiconductor materials. Each material has its unique strengths and characteristics which influence its suitability for specific applications. For example, quantum dot sensitization, dye sensitization, thin-film silicon, organic heterojunction, group II/V/VI thin-film semiconductors, and other current light-absorbing materials have intensively been studied for the fabrication of cells.[2] However, there is a gap in the market for next-generation sustainable PV cell materials that are not solely highly efficient in light absorption and conversion but also sufficiently inexpensive and environmentally stable.[4] Specific PV cell materials exhibit varying operating performances on their crystallinity, bandgap, absorption, and manufacturing complexity. As illustrated in figure 1.2, photovoltaics is usually divided into three main generations, which are well-developed and utilized for several years. The 1st Generation (*traditional*) photovoltaics belong to current generation and

are made of Silicon or Germanium, doped with phosphorous and boron in Pn-junction. The 2nd Generation photovoltaics, called thin-film solar cells, are made of many tiny crystalline grains of semiconductor materials. The materials used in these cells have properties that are different than those of silicon. Thin-film cells have advantages over their thick-film counterparts. The 3rd Generation solar cells are made from variety of materials besides silicon. These include solar inks using conventional printing press technologies, solar dyes, and conductive plastics. More developed solar cells use plastic lenses or mirrors to concentrate sunlight onto a minuscule area of high-efficiency PV material. These PV materials are more expensive and therefore cannot be used for general purposes. Last but not least, perovskite-based solar cells recently emerged as the fourth generation of photovoltaic technology which exceeded expectations in terms of producing high power conversion efficiency in a very short period.[5]

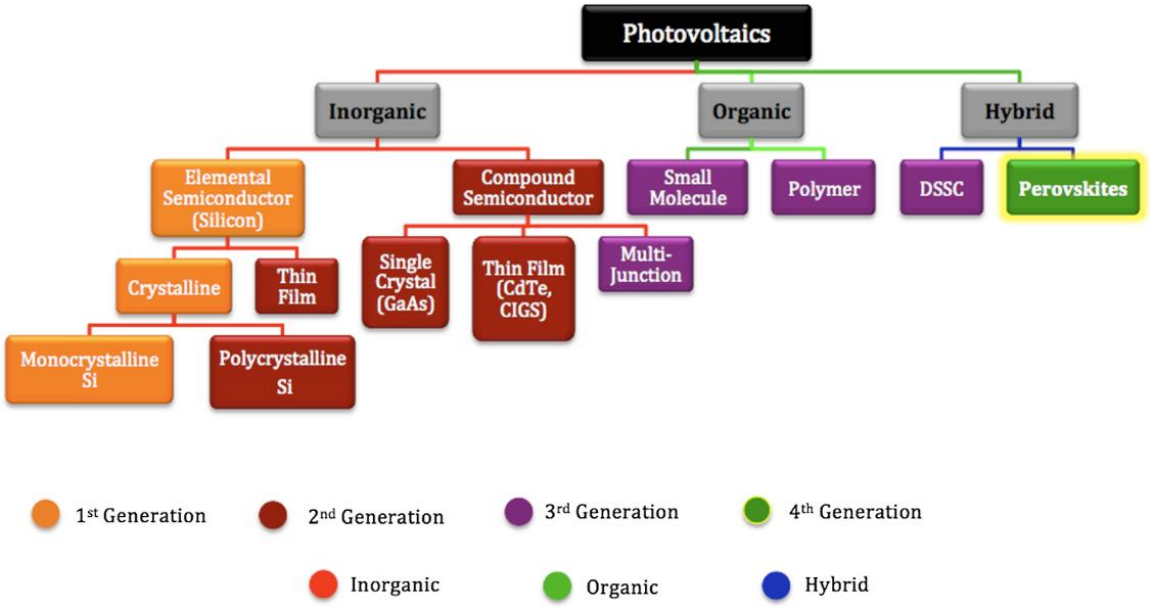

Figure 1.2: Evolution of photovoltaic solar cells [6]

A significant amount of attention has been given to hybrid metal halide perovskites, with the typical structure composed of five layers depicted in figure 1.1, due to the simple preparation along with its magnificent optoelectronic properties[5]. This material has gone from power conversion efficiencies (PCE) of 3.81% (X=I) and 3.13% (X=Br)[2] to recent following improvement in performance in state-of-the-art devices; 22 %.[6] The most widely investigated organolead halide perovskites are $CH_3NH_3PbI_3$ and $CH_3NH_3PbI_{3-x}Cl_x$ because of their long carrier diffusion length in the order of 100 nm and over 1μm, respectively. The long carrier diffusion length plays a key role in allowing sufficient light absorption and efficient charge transport/extraction to achieve high photocurrents. They have high carrier mobility of about 66

$cm^2/V.s$ which significantly reduces carriers recombination. The large-scale commercialization of these perovskite solar cells is however impeded by the instability of the perovskite medium and difficulty in reproducing the device [7]. Addressing this stability has thus become a hot research topic over the past decade. Theoretically, thin-film solar cell performance is influenced by characteristics of the absorber layer such as morphology, thickness, composition of precursors, compactness, and deposition method. In this study, materials of the hole transporting layer (HTL), electron transporting layer (ETL), and absorbing layer are investigated to determine the combination of materials to fabricate efficient PSCs.

1.2. Research Aims and Objectives

1. Synthesis, characterization, investigation, and optimization of the HTMs, ETL materials, and the Perovskite layers.
2. Perovskite device elaboration with studied p- and e-type semiconductor layers
3. To compare and determine which is the best combination of materials to develop an inexpensive, efficient, and stable solar cell
4. To test the application of the solar cells by subjecting them to a simulation
5. To author a full-length research publication to present the main results and outcomes from the synthesis, characterization, and application procedures

1.3. Hypothesis

The cells containing SnO_2/$MAPbI_3$ will display better device performances than their counterparts and can be determined using J-V curve testing.

1.4. Research Questions

1. Which combination of materials will yield the best PCE?
2. Will terephthalic acid (TPA) stop or reduce the degradation of $MAPbI_3$?
3. Will chlorobenzene (CB) stop or reduce the degradation of $MAPbBr_3$?
4. Is reduced graphene oxide a good alternative to its expensive counterpart spiro-OMeTAD?

1.5. Research Approach

In this study, background knowledge was obtained by constructing a literature review, which helped to determine the best-proposed materials and methods to fabricate cheaper alternative PSCs, suitable for stable energy conversion processes. Experimental procedures were designed, and the steps were followed to study The Nano-optimization of P- and E-type Semiconductor Films for Efficient Perovskite Photovoltaics. These steps included:

A) The synthesis of ETMs (ZnO and SnO_2), HTMs (rGO), and perovskites ($MAPbI_3$ and $MAPbBr_3$).
B) The technique and its parameters to deposit these materials onto the ITO coated substrate.
C) The characterization and optimization of the materials.

For the characterization of the materials, the materials were spin-coated onto ITO-coated substrates. With regards to the spin-coating process, the amount of material used, the spin-coating speed, deposition time, and the annealing temperature and time were taken into consideration.

The ETMs (ZnO and SnO_2), HTMs (rGO), and perovskites ($MAPbI_3$ and $MAPbBr_3$), were characterized using HRSEM, XRD, XPS, FTIR, UV-vis, PL, CV, and EIS. These characterization techniques were employed to study the structural, morphological, electrical, and optical properties of the synthesized materials. Consequently, these techniques were used to optimize the different layers of the PSC.

J-V measurements were carried out during the application part of the project to determine the efficiencies of the PSCs and the performance was analyzed.

1.6. Thesis Outline

The following thesis consists of six chapters detailed as follows:

Chapter 1: contains a brief introduction to solar cells, the introduction of perovskites in solar cells, their structure, and the principle of the photovoltaic effect. Furthermore, the questions motivating this project are asked, as well as the aims and objectives laid out.

Chapter 2: the motivation behind this project is introduced, followed by the generations of solar cells, before elaborating on perovskite solar cells. The operating principle of perovskite solar cells is then discussed before the different materials previously and currently used in the fabrication of PSCs are presented, as well as the different deposition methods used in the fabrication process.

Chapter 3 : consists of a list of materials used in this project, along with the synthesis, and characterization of the materials. The parameters used for the fabrication of the PSCs are detailed within the chapter, as well as a brief description of the characterization techniques and the instruments used

Chapter 4: the results and discussion section detailing the outcomes of the characterization techniques are presented. The characterization techniques, include, HRSEM, XRD, FTIR, XPS, UV-vis, PL, CV, EIS, and J-V curves. The degradation of the perovskites and the application of the PSCs are discussed.

Chapter 5: contains a summary of the outcomes obtained in the thesis, concluding the work. Furthermore, recommendations based on possible future work are mentioned based on this study.

CHAPTER TWO

Literature Review

The following chapter illustrates the motivation behind this project, namely, the energy crisis, followed by the previous generations of solar cells, before elaborating on perovskite solar cells. The operating principle of perovskite solar cells is then discussed along with the different materials previously and currently used in the fabrication of PSCs. Concomitantly, the various preferred methods used for deposition in the fabrication process are highlighted.

2.1. Energy crisis

The energy crisis is one of the most critical issues that need attention in this 21st century. The growing energy demand is undeniable and the non-renewable resources available to sustain this demand are depleting. The best alternative solution has always been renewable energy. Over the last decade, developing countries have been pressured into the increased implementation of alternative sources of energy due to population growth and economic development [8].

South Africa, in particular, having a developing and emerging economy, is currently faced with a two-fold energy challenge; meeting the needs of millions of people who still lack access to basic, modern energy services while simultaneously participating in a global transition to clean, low-carbon energy systems [9].

According to Jain *et* al., South Africa is the 7th largest coal producer and the 5th largest exporter of coal in the world. Approximately 77% of South Africa's energy needs are obtained from coal, a majority of which is used for power generation. Consequently, the annual CO_2 emissions of 437.37 Mt or emissions of 8.10 t CO_2 per capita per annum make South Africa the highest contributor to greenhouse gas emissions in Africa [10].

Thus, the need to move towards solar energy conversion at a progressive pace cannot be over-emphasized. The use of solar energy is a favourable option for multiple reasons:

I. Solar energy is the most abundant renewable energy as the sun emits approximately 3.8×10^{23} kW of which the earth intercepts 1.8×10^{14} kW. It reaches the earth in forms such as light and heat, however, the majority is lost due to absorption, scattering, and reflection by clouds [11].

II. Solar energy is an auspicious energy, as it is inexhaustible and presents solid and increasing output efficiencies. Two factors that determine efficiency in the solar PV industry are solar radiation intensity and distribution. Most developing countries receive solar radiation in advantageous quantities [12], as shown in Figure 2.1.

III. The application and pursuit of solar energy do not have a damaging effect on the ecosystem [13].

IV. A solar system can be used for village systems, industrial operations, and homes, as it is affordable, reliable, and applicable [14].

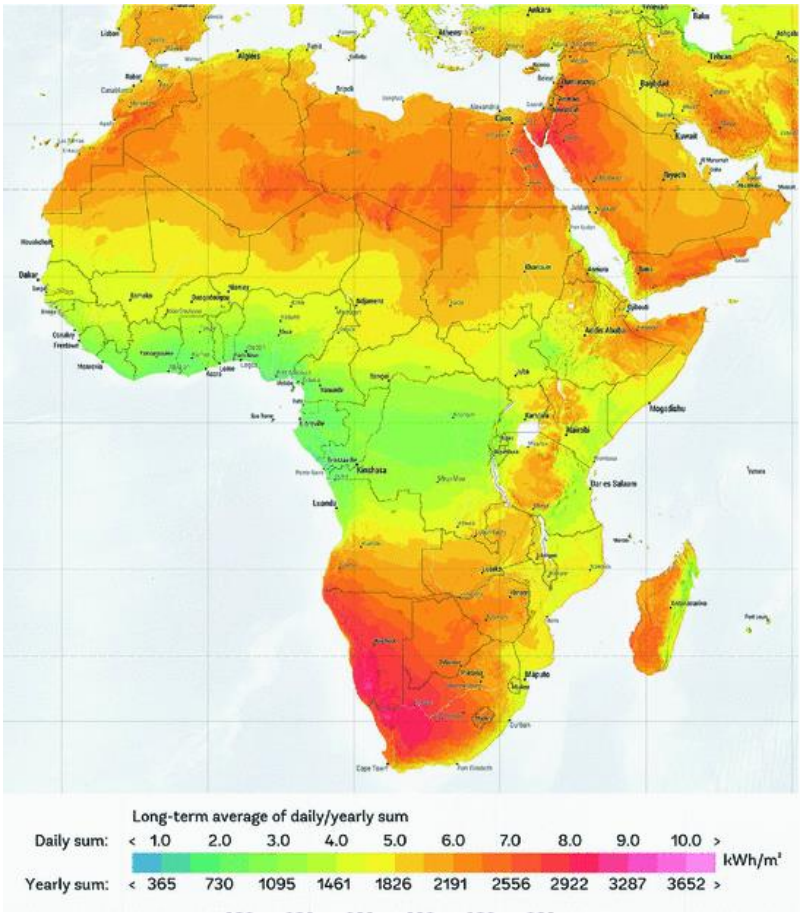

Figure 2.1: Illustration of Africa's photovoltaic power potential[15]

The growing demand experienced in many developing countries including South Africa can be fulfilled with the use of solar energy as it is abundant in nature and freely accessible at no additional cost [8]. South Africa has the 3rd largest solar resource in the world, with an average of more than 2500 hours of sunshine per annum, with daily solar radiation levels between 4.5 and 6.5 kWh/m^2 [16]. Photovoltaic cells are the most rational choice to resolve the world's energy crisis. However, the cost of photovoltaic cells is quite high, but have high energy outputs due to the relatively high solar intensities, making solar power the option of interest [17].

2.2. Solar cells

Solar cells are designed to convert sunlight into electrical energy using their photovoltaic properties. They are nearly permanent as they have an uninterrupted source of power, with minimal operating costs. Solar cells convert solar energy directly into electricity without an intermediate energy form [18].

As mentioned in section 1.1 and illustrated in figure 2.2., there are three generations of solar cells, each having a specific chemical composition, structure, corresponding efficiencies, and cost [19]. These three generations of solar cells are briefly discussed in the subsections below.

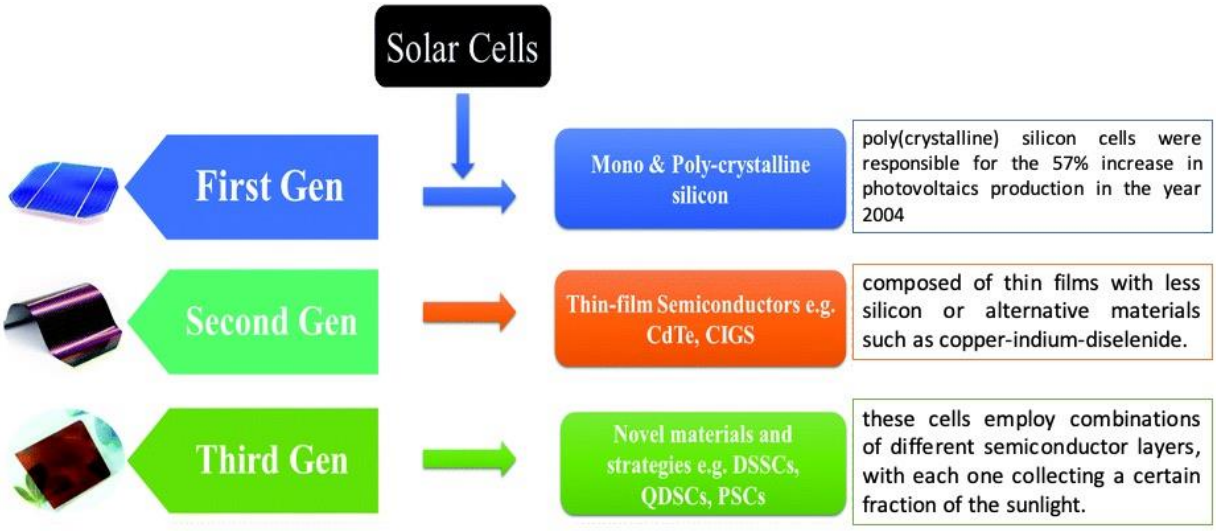

Figure 2.2: The different generations of solar cells[20].

2.2.1. 1st Generation cells

First-generation cells are made of crystalline silicon, as illustrated in figure 2.3. These cells can either be monocrystalline or polycrystalline. Monocrystalline solar cells consist of silicon positive-negative (Si p-n) junctions and managed to attain an efficiency of 25%, whereas polycrystalline solar cells are produced by melting silicon and solidifying it to position crystals in a secured direction to develop multi-crystalline Si, which is carved into thin wafers. Polycrystalline solar cells' efficiency is less than that of monocrystalline solar cells, but has low production costs and less number of defects in the crystal structure. Monocrystalline and polycrystalline solar cells are an established and commercial technology for the broad absorption of the solar spectrum, with high carrier mobility. However, the production of these cells is quite expensive with complicated processing impeding the global application of these solar cells [20].

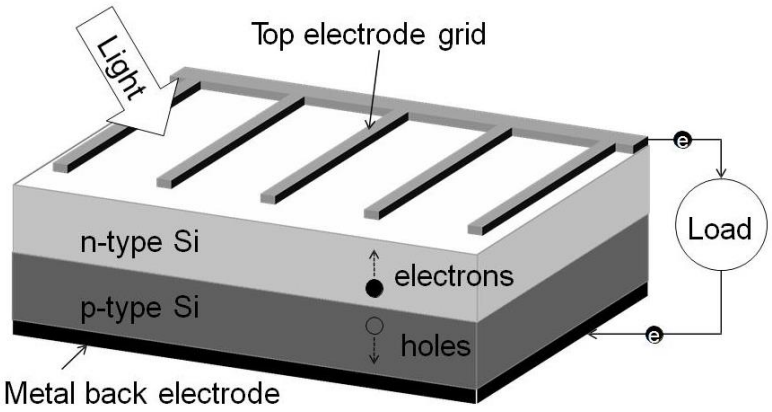

Figure 2.3.: Diagram of a first-generation solar cell [21]

An alternative to crystalline silicon cells has been proposed, such as emitter wrap-through (EWT) cells, which consist of laser-drilled holes in the front and back surfaces of the cell to increase the surface area, resulting in the enhancement of the absorption of solar radiation. This cell design results in higher efficiency and lower production cost. The EWT cells are more efficient at lower temperatures and require less area for a given unit, however, the performance decreases at high temperatures [22].

2.2.2. 2nd Generation cells

Figure 2.4. below, illustrates a second-generation PV cell which consists of thin-film cells. They are cheaper than first-generation cells as they use less silicon material. However, they make up less of the PV market due to them having a lower efficiency than first-generation cells. There are multiple variations of thin-film cells; one of those being amorphous silicon (AS) solar cells. AS cells are inexpensive due to the small amounts of material used and the ability of roll-to-roll production of modules. However, they have significant disadvantage, such as low efficiency with instability affecting the electrical output with time [22].

Second-generation solar cells are produced using methods such as, chemical vapour or vapour-assisted deposition. Other than AS solar cells, second-generation solar cells include copper-indium-gallium-selenide (CIGS) technology. These materials have the potential to be made thinner and lighter which is an advantage that the silicon counterpart does not have [23].

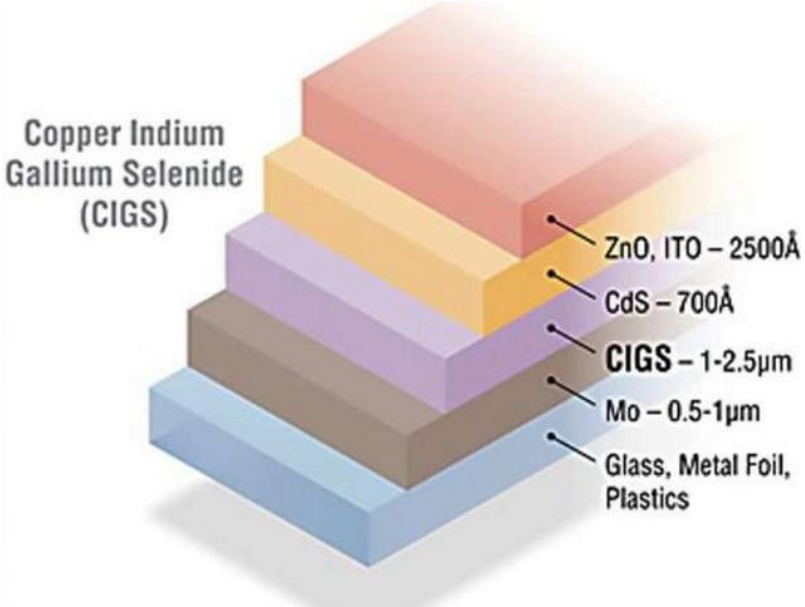

Figure 2.4: Diagram of a second-generation solar cell [24].

2.2.3. 3rd Generation cells

The improvement of second-generation solar cells led to the development of third-generation low cost, environmentally friendly solar cells with higher efficiency. These solar cells use nanostructures to optimize absorption, carrier generation, and separation [22]. Figure 2.5 displays a typical third generation solar cell.

Third-generation solar cells focus on minimizing the use of materials and minerals that require a lot of refinement, such as silicon. These solar cells employ organic molecules with high molecular weight, such as perovskite, as semiconductors. Perovskite photovoltaics use metal-halide or organometallic materials which produce power conversion efficiencies comparable to those produced by silicon solar cells and at a cost lower due to the simplified production process [25].

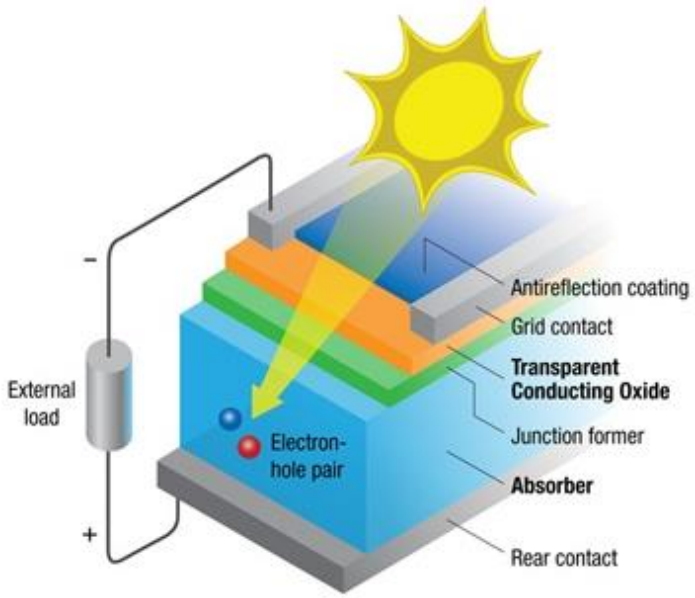

Figure 2.5: Diagram of a third-generation solar cell [26]

2.3. Perovskite

Perovskite solar cells (PSCs) have gained a lot of attraction due to the outstanding optoelectric properties, such as, the high carrier diffusion length and strong absorption. They can be produced via the multiple existing, inexpensive production methods using flexible materials [27].

Perovskites are compounds that are defined using the formula ABX_3, in which X represents a halogen such as Br^-, I^- or Cl^- and A and B are different sized cations as illustrated by figure 2.6.

PSCs hold multiple advantages over the conventional thin film and silicon solar cells, such as low cost, simple processing steps at low temperature and enhanced efficiencies up to 31%. The main advantage, however, is that PSCs can perform all three tasks required for the operation of solar cells, which include; light-harvesting, charge generation, and transport [28, 29].

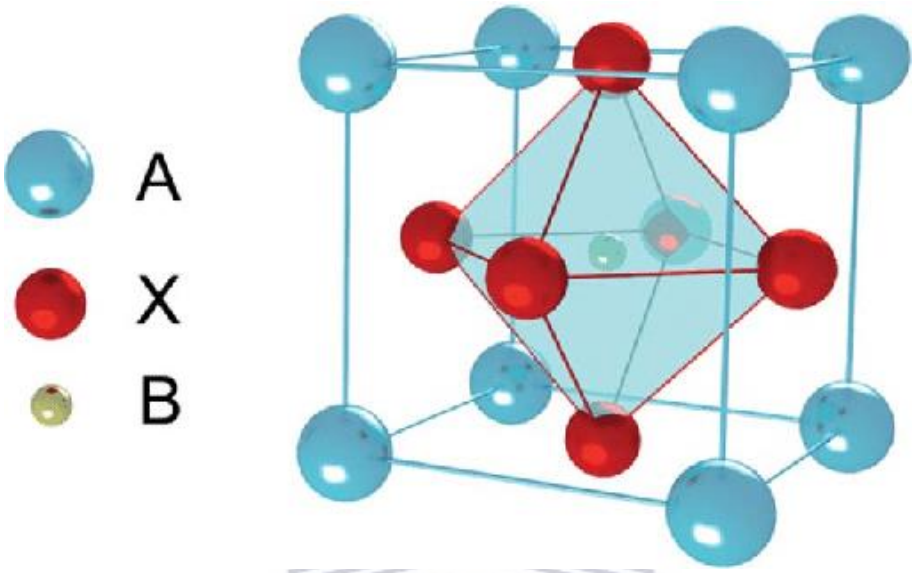

Figure 2.6: Schematic illustration of a perovskite nanoparticle, in our case, 'A' is methylammonium, 'B' is Pb and 'X' is a halogen [30].

Despite the multiple favourable characteristics, unfavourable characteristics are preventing the commercialization of these solar cells. These include the scaling up of the spin-coating process, the stability of the cells, the toxicity because of the lead compounds used in the cells, and hysteresis in J-V curves. Structural stability refers to the capability of the crystalline stage to resist degradation over a wide range of external factors, moisture, pressure, and heat [23, 27]. For instance, $MAPbI_3$ is much more sensitive to environmental factors compared to $MAPbBr_3$ [31]. The material decomposition, degradation study linked the stability of $MAPbBr_3$ to a prevalence of a reversible decomposition reaction;

$$CH_3NH_3PbX_3\ (s) \rightleftharpoons CH_3NH_2\ (g) + HX\ (g) + PbX_2\ (s), \qquad \text{(Reaction 1)}$$

in comparison to the irreversible decomposition pathway

$$CH_3NH_3PbX_3\ (s) \rightleftharpoons NH_3\ (g) + CH_3X\ (g) + PbX_2\ (s), \qquad \text{(Reaction 2)}$$

compared to $MAPbI_3$ which displays both decomposition types. The decomposition reaction,

$$4CH_3NH_3PbX_3 + O_2 \rightleftharpoons 4PbX_2 + 2X_2 + 2H_2O + 4CH_3NH_2 \qquad \text{(Reaction 3)}$$

indicates that it slows down upon the substitution of iodide with bromide [31].

According to Olaleru *et* al., working principles of the PSCs are crucial to pinpoint the physical procedures that restrict the performance of the photovoltaic device. Unfortunately, the acquired knowledge from predecessor solar cell technology cannot always be applied to the perovskite

equivalents. $MAPbI_3$ is one of the first perovskite compounds that excited the PV research field, due to its favourable optoelectric properties which are rarely seen [32], in comparison to $MAPbBr_3$, which has not received much attention. According to Riet *et* al., the investigation of the optical properties of $MAPbBr_3$ could play a key part in solving the low-efficiency problem displayed by the material in solar cells [33].

Therefore, knowing the working principle of the PSCs will make it possible to determine the photovoltaic parameters necessary to define the efficiency, such as the fill factor (FF), open circuit potential (V_{oc}), and short circuit current (J_{sc}).[23]

Table 2.1 depicts the photovoltaic parameters of $MAPbI_3$ and $MAPbBr_3$, in which the cell containing $MAPbI_3$ generates a V_{OC} of 1.00 V, FF of 0.681, and short-circuit photocurrent density of 21.7 $mA.cm^{-2}$, compared to $MAPbBr_3$ generating a V_{OC} of 1.082 V, FF of 0.59 and short-circuit photocurrent density of 10.85 $mA.cm^{-2}$ which is double that of $MAPbI_3$. According to Wu *et* al., this generally occurs for thick planar perovskite layers which are associated with the dielectric properties of the ionic crystal [34].

Table 2.1: Photovoltaic parameters of perovskites in PSCs

Sample	Open circuit potential (V_{OC})	Fill Factor (FF)	Short circuit current (J_{sc})	Power Conversion Efficiency (PCE)	References
$MAPbI_3$	1.00 V	0.681	21.7 $mA.cm^{-2}$	14.8 %	[34]
$MAPbBr_3$	1.082 V	0.59	10.85 $mA.cm^{-2}$	6.93 %	[35]

2.3.1. Operating principle

As illustrated in figure 2.7. below, when a light source emits photons, it reaches the perovskite layer through the glass and transparent electrode. The photon is then absorbed by the active layer and if the photon energy is higher than the energy gap of the perovskite material, the creation of exciton will occur. The exciton will be separated by the internal potential to free charge carriers from the work function difference between the metallic electrode and transparent electrode. The holes will be transported to the HTL and the electrons to the ETL, and eventually the holes to the metallic electrode and the electrons to the transparent electrode [36].

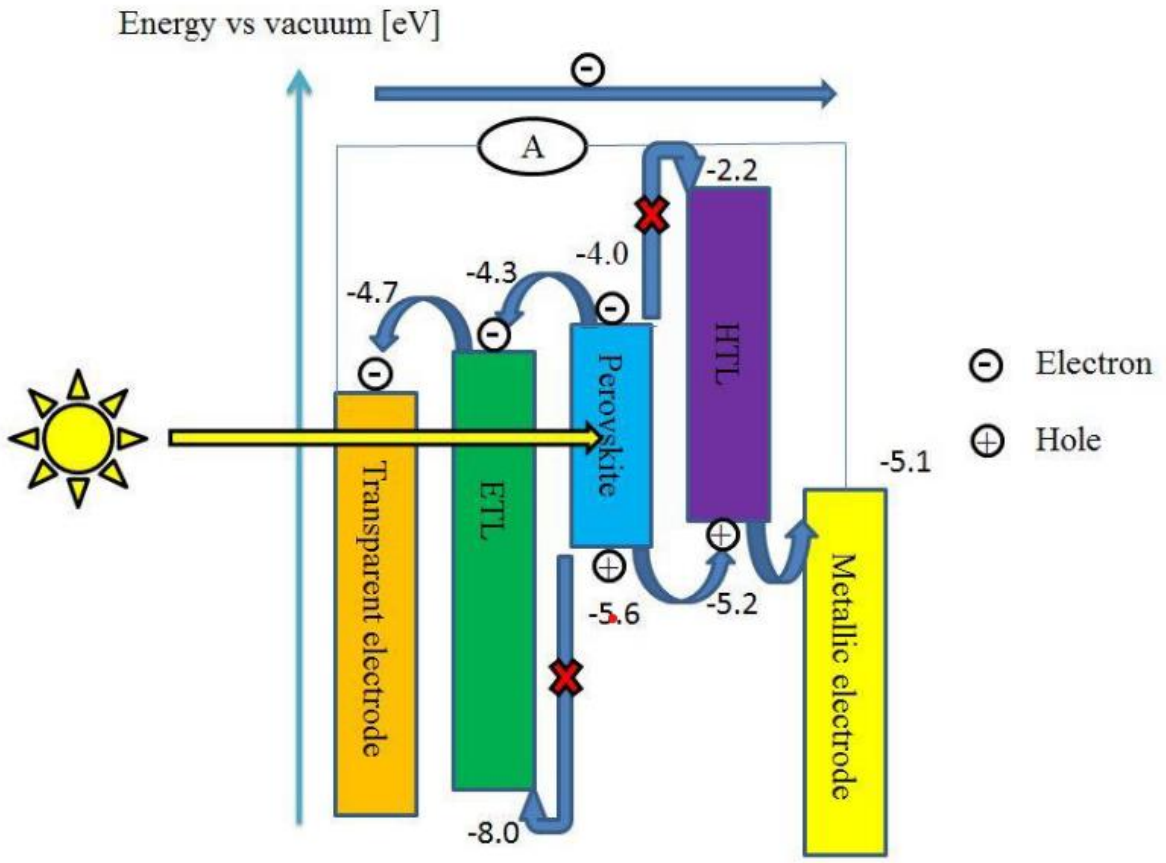

Figure 2.7: Schematic of an energy band diagram illustrating how PSCs operate [36].

Two of the crucial characteristics of PSCs that explain their achievements are the low exciton binding energy and absorption properties. The first physical phenomenon in the generation of photovoltaics is light absorption. The photon, with energy greater than the bandgap, excites the active material creating an electron-hole pair. When the generation of the holes and electrons are completed in the perovskite, they will be collected by the contacts after it reaches the contacts, which is a process related to the charge-transfer properties of the halide perovskite. The power conversion efficiency (PCE) of perovskite solar cells containing metal halides is a result of the materials' charge-transport properties with a long charge carrier diffusion length [23].

There are four cases related to the morphology of the sample that can coincide within the perovskite device, namely;

i. The perovskite is generally deposited onto the metal oxide with a thickness of a few nanometres (200 – 400 nm) as a thin light-harvesting film.

ii. The perovskite is partially not in direct contact with the oxide substrate, however, is present in the pores and capping layer which is situated above the mesoporous network in the form of isolated crystalline domains.

With the addition of the hole-transporting material (HTM), the previous two cases can be paired with the following cases:

iii. The HTM is deposited into the pores, creating a continuous union with the perovskite material.

iv. There will be limited HTM present in the pores or the interfacial contact located between the HTM and perovskite is only limited due to infiltration problems [37].

The perovskite film morphology is linked to three competing mechanisms: (i) the formation of the photo-induced trap state, (ii) the passivation of these trap states, and (iii) the perovskite degradation. In order to improve these mechanisms an anti-solvent can be utilized such as chlorobenzene in the case of $MAPbBr_3$ [33]. However, according to Hou *et* al., in the case of $MAPbI_3$, terephthalic acid (TPA) was utilized as an additive to promote lateral growth of the perovskite grains to lower the nucleation free-energy to better the competing mechanisms [38]. The highest PCEs achieved by PSCs with the formula ABX_3, which mainly uses iodide derivatives, have bandgaps of approximately 1.5-1.6 eV. On the other hand, PSCs using methylammonium lead bromide material have a bandgap of 2.3 eV, which can produce higher open-circuit voltages (V_{oc})[39].

2.4. Methods of perovskite film preparation

The two major mechanisms used in the preparation of perovskite films are vacuum deposition and solution processing. Solution processing methods have a preferential advantage over vacuum deposition because of the low cost and compatibility with roll-to-roll device production. In both cases, researchers used various steps or procedures in the preparation of the films that resulted in a difference in the quality of the film as well as in the reported power conversion efficiencies. Common procedures in vacuum deposition are one-step precursor deposition, sequential vapour deposition, and dual-source vacuum deposition processes. While in the solution processing approach, one-step spin-coating, two-step spin-coating, vapour-assisted solution processing, and spray-coating are some of the most common deposition methods. A brief account of each deposition method will be discussed in the following subsection.

2.4.1. One-step method

The one-step spin-coating method consists of all perovskite precursors in a single solution, which will be deposited onto the substrate before a thermal annealing is applied (see fig. 2.8)[40]. The spin-coating process involves the deposition of the perovskite solution onto the necessary substrate, after which the substrate is rotated at high speed and following a drying step. The thickness of the film is determined by the parameters, namely, the viscosity of the solution, spinning velocity, and temperature. Once the spin-coating process is completed, the substrate is generally annealed to promote the evaporation of the residual solvent and improve the crystallinity [41]. This solution contains a mixture of organic and inorganic precursors, and since these hybrid materials have rapid crystallization times, the method yields a high density of pinholes in the resulting coated perovskite film, reducing the number of photogenerated charges, which leads to a low short circuit density and PCE [42]. This method is quite simple and is relatively common for particular perovskite compositions as the precursors might undergo certain chemical reactions in the solution, which can influence the resulting film and the performance of the devices.[40] To assist with the formation of easy high-quality perovskite films, anti-solvents such as chlorobenzene or diethyl ether, can be added to the films during the spin coating process [40–42].

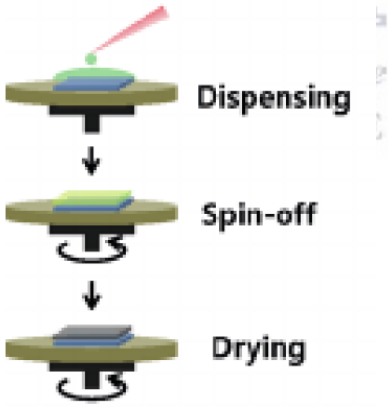

Figure 2.8: Illustration of the one-step deposition method [43].

2.4.2. Two-step method

In this method, one of the precursors is first deposited, after which, the second precursor is deposited and thermally annealed. Generally, the first precursor is deposited using the spin-coating method, whereas the second precursor can be deposited using the spin-coating method or by dipping the substrate into a solution, as illustrated in figure 2.9 [40].

The two-step method was developed to improve the film coverage, in which the organic and inorganic precursors were coated sequentially and annealed at a temperature of 70-100 °C to drive the inter-diffusion to form perovskite films.

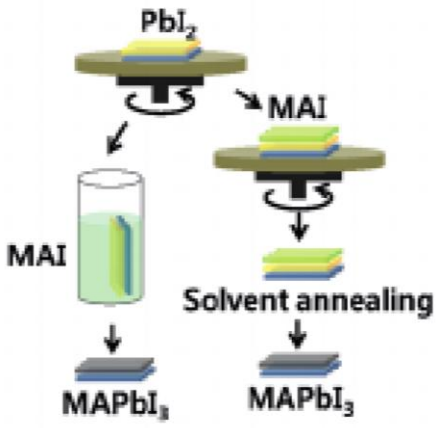

Figure 2.9: Diagram depicting the two-step or sequential deposition method [43].

In the two-step process, the in-solution conversion is suppressed. Therefore, after the deposition of both solutions separately, full mixing and sufficient mass transfer between the two precursor solutions are necessary. According to Habibi *et* al., the spin/dip combination is an efficient procedure for the fabrication of the perovskite crystals in mesoporous scaffolds, as the dipping process promotes the infiltration of the MAI solution into the scaffold pores [44].

2.4.3. Spray coating

Spray-coating employs solution-based deposition technique that results in a reduction of material wastage, roll-to-roll compatibility, and high-throughput processing [45]. Spray coating is commonly used in the synthesis of perovskite oxides, where the thin-film deposition, as illustrated in figure 2.10, is achieved by spraying the solution onto the substrate, after which a chemical reaction takes place between the constituents in the system forming the layer. The solution used for coating is created in a way in which all unwanted products are volatile at working temperatures [41].

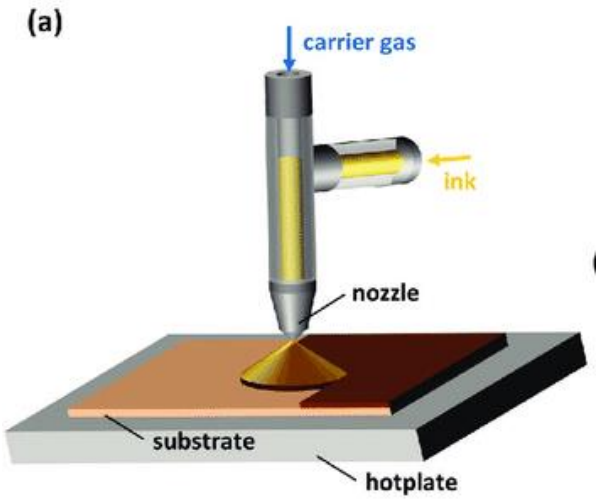

Figure 2.10: Illustration of the spray coating process [45].

In the spray coating process, the precursor solutions can be extra-dilute, allowing the processing of poorly insoluble or soluble materials. This deposition process involves several parallel and sequential steps, such as, the atomization of a liquid solution, droplet impingement on the substrate surface, droplet flight and evaporation, crystallization, wetting, drying, and film formation.[44]

Spray coating is the fastest method used to obtain scalable perovskite layers to provide a high coating rate in a continuous process [46]. For instance, Yun *et* al. displayed a spray coating technique based on the crystallization of the antisolvent. The spray antisolvent method facilitates the fabrication of large-area perovskite films of high quality [47]. However, spray coating is not generally used as it is performed under ambient conditions, which may disturb sensitive precursor materials [48].

2.4.4. Vacuum Deposition

Thermal evaporation, also known as vacuum deposition, is a technique in which the material is directly deposited from the vapour phase. As illustrated in figure 2.11, during the deposition process, precursor is heated to a high evaporation temperature to induce vaporization, the substrate is maintained at low temperature [41].

Multiple variations of deposition of perovskite layers using thermal evaporation have been produced, which include single-source evaporation [48, 49], sequential evaporation [50, 51], and multiple source co-evaporation [52]. Single-source evaporation is made possible by combining the precursors of the perovskite in a crucible or by preparing the perovskite crystals that are ground into a powder for evaporation. Sequential evaporation pursues a similar method to that of the two-step solution-processed deposition, in which each precursor is separately

evaporated, followed by thermal annealing. Multisource evaporation is the most commonly used method, in which each precursors are placed in separate crucibles and are co-evaporated simultaneously along with the other precursors to form the perovskite layer [40].

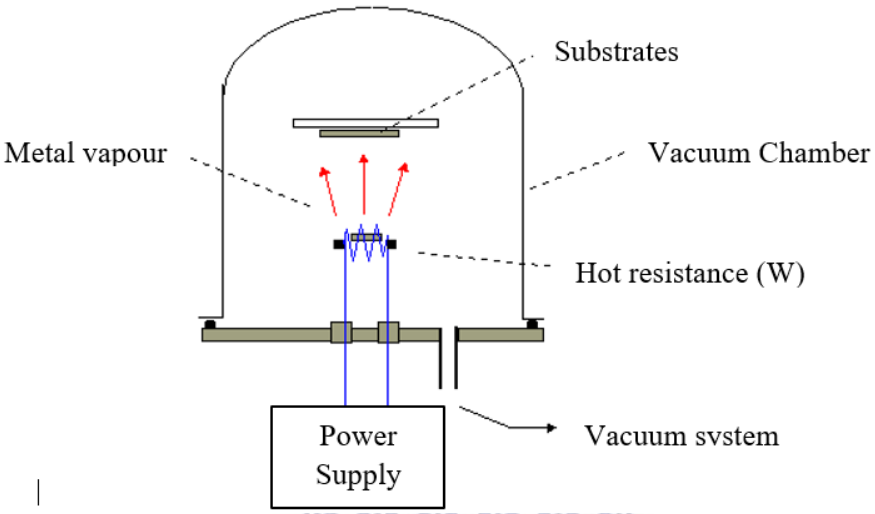

Figure 2.11: Illustration depicting a single-source thermal evaporation set-up [53].

The simplicity of fabrication has favoured the use of lab-scale solution-processing methods, resulting in high-performance devices. However, most of these methods are not directly relevant to a larger scale and volume preparations, impeding the incorporation and market entry of these materials. Vacuum methods provide advantages in the deposition of perovskite thin films, which include the intrinsic purity of sublimed materials, the low substrate fabrication temperature, and the control over the film thickness [54].

The challenges that vapour deposition face includes, optimizing the source evaporation, the rate, and growth processes and developing solutions that prevent source banter of volatile substances [55].

Vacuum deposition techniques are intrinsically additive, meaning multilayer devices can be built without the need for chemical modifications of the underlying layers or the need for orthogonal solvents and can be utilized to deposit highly crystalline perovskite films at room temperature [56]. The formation of thermal vacuum-deposited perovskite films, differs significantly from solution-processed films due to the absence of solvents, intermediate species, and the distinctive crystallization kinetics as a function of temperature and stoichiometry [57].

Organo-halide perovskites are generally prepared in a high vacuum chamber, utilizing three different thermal sources, each source is equipped with a crucible and a quartz crystal microbalance (QCM) sensor, as illustrated in figure 2.12 [58].

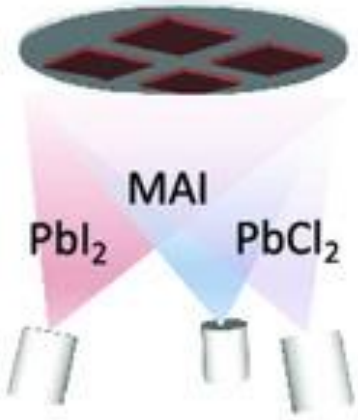

Figure 2.12: Schematic of a three-source vacuum deposition of an organo-halide perovskite [58].

The thickness and deposition rate of the layers are monitored using the quartz oscillator microbalances. Experiments that utilize the vacuum deposition method maintain the stoichiometry of the precursors during deposition, therefore, an annealing step is not required to fully convert the as-deposited films to the perovskite structure [56].

2.5. Hole transporting materials (HTMs)

PSCs use hole transporting materials (HTMs) to effectively collect and transport the holes extracted from the light harvest layer of the perovskite to the anodes [59].

The HTL plays a critical role in solar cell performance [60]. Spiro-OMeTAD remains the HTL of choice with the best-reported performance until very recently. However, Spiro-OMeTAD is prohibitively expensive. It is also a poor conductor, and thus, requires a complicated doping process that is difficult to control [61]. There is a renewed interest in identifying alternative HTMs, other than spiro-OMeTAD that can yield high PCEs [62]. HTMs utilized in PSCs are mainly organic semiconductors due to their meeker processing conditions agreeable with perovskites. However, HTMs display moderately low hole mobility, due to their organic nature, therefore, the presence of a dopant is required [63].

Thermal stability enhancement in solar cells is crucial for the commercialization of PSCs. Jeon *et* al. stated that most devices that would utilize spiro-OMeTAD as an HTM are linked to the

severe degradation against thermal stress due to the additives resulting in an outstanding drop in glass transition temperature (T_g) of the HTM [64].

Spiro-OMeTAD displays low electrical conductivity in its pristine form, as it has an amorphous nature, therefore, doping is required to overcome this limitation to increase the hole charge density. Tert-butylpyridine (TBP) is generally used for the doping process, increasing the polarity of the HTM, and simultaneously improving the contact between the perovskite and the latter. The doping strategy also happens to rely on the manipulation of lithium Bis(Trifluoromethanesulfonyl)Imide (Li-TFSI) to accomplish low series resistances in the solar cells, by oxidizing (p-doping) spiro-OMeTAD, in which the lithium ions will be consumed while the reaction progresses, indicating that Li-TFSI acts a reagent [65].

However, doped spiro-OMeTAD tends to suffer degradation as well. Once Li-TFSI is exposed to humidity or high temperatures, it generally dissociates from the spiro-OMeTAD, reducing its desired effect. In the case of TBP, due to it being a polar solvent, as the nature of the solvents used for perovskite deposition, the TBP would corrode the perovskite absorption layer, affecting the PSCs stability. Therefore, a low-cost, doping-free HTM is needed to maintain the cell performance over time, to further develop the PSC technology [65].

Table 2.2: Summary of HTMs performance parameters

HTM	**Performance Parameters**						**References**
	FF (%)	J_{SC} ($mA.cm^{-2}$)	V_{OC} (V)	PCE (%)	Band gap energy (eV)	Hole mobility ($cm^2\ V^{-1}\ s^{-1}$)	
rGO	48.4 ± 3.5	13.5 ± 1.2	0.57 ± 0.005	3.5 ± 0.4	3.09 ±0.04	123	[66], [67]
Spiro-OMeTAD	84.81	22.81	1.02	19.77	3	2×10^{-4}	[68]

Reduced graphene oxide (rGO) typically aids an efficient semiconductor with an adjustable work function in the range of 4.4-4.9 eV, showing multiple functions such as an electron transport material (ETM) and a hole-transport material (HTM). The optical and electronic properties of rGO are easily diversified by chemical functionalization, enabling functionalized rGO to meet certain demands [69]. rGO displays superior electrical properties compared to

graphene oxide and can be dispersed in polar solvents, as opposed to hydrophobic graphene, due to the presence of oxygen moieties. rGO displays outstanding mechanical, chemical, and thermal stability. A crucial parameter that determines the selectivity of rGO is the work function, which is regulated by the oxygen concentration, ranging from 4.35-5.28 eV. Due to its high work function, rGO has frequently been used as a substitute for conventional HTMs for stable PSCs. Kim *et* al. state that rGO has been found to minimize the defects of the perovskite layer by participating in the perovskite formation process, while simultaneously suppressing the recombination at the interface by passivating the defects [68, 69].

Huang *et* al. reported an environmentally friendly thermal reduction method using N_2. The GO was placed in a furnace filled with N_2 and thermally reduced to 200 °C. The HTM increased the open-circuit voltage to 0.95 V, with a relative power conversion efficiency of 10.5 % with high reproducibility [59].

According to Feng et al, high-quality rGO can be produced using a sodium-ammonia (Na-NH_3) system. A Na-NH_3 solution can be employed to successfully reduce GO, resulting in the restoration of the graphene structure at low temperatures, leading to the production of rGO with high carrier mobility of 123 cm^2Vs^{-1} and low oxygen content of 5.6 wt%, within minutes. The rGO film can be directly produced onto the substrate due to the low-temperature reduction process, with a low sheet resistance by submerging the GO film in the Na-NH_3 solution for several minutes. In comparison to alternative methods, this method produces rGO with high conductivity in a short time, a low number of remaining functional groups, and low processing temperatures, resulting in a more environmentally-friendly method [70].

2.6. Electron Transport Layer of Perovskite Solar Cells

ETLs is used to collect and transport electrons to the cathode. Semiconductors, such as TiO_2 and ZnO, have been presented as favorable materials in the application of solar cells. SnO_2 thin films are spin-coated using crystalline NPs allowing efficient electron extraction without the need for high-temperature post-treatment [71]. A variety of nanostructures of these materials have been produced, including nanotubes, nanorods, nanofibers, and nanowires. Additionally, other materials have been utilized as photoanodes, such as SnO_2 due to its wide bandgap and high mobility [72].

TiO_2 is the conventional ETM that is commonly used for PSCs, however, due to its low mobility, it is not an ideal material. In the fabricating process of TiO_2, high annealing temperatures are used to decompose the organic titanium precursor into anatase TiO_2, but this

leads to the decomposition of the perovskite layer and difficulty in tightly contacting the compact layer to the mesoporous layer, which may result in the splitting of the TiO_2 from the substrate (FTO, ITO, etc.) [73].

According to Wang *et* al., low-temperature SnO_2 has a wider bandgap, and high electron mobility in comparison to high-temperature SnO_2, resulting in low-temperature PSCs performing better than high-temperature PSCs. To solve possible low voltage in SnO_2 PSCs, as a result of the deep conductive band edge of SnO_2, surface passivation of SnO_2/perovskite interface is carried out to maintain perovskite crystallinity [73].

The energy level of SnO_2 is less than that of ZnO and TiO_2, suggesting that the electrons injected from the absorbing layer to SnO_2 are faster than their counterparts. Due to its high electron mobility, SnO_2 could help extract and transport electrons from the absorbing layer to the collecting electrode [74].

According to Song et al., SnO_2 thin films could present sufficient conductivity without the need of high-temperature sintering process. This will benefit future fabrication of photovoltaic devices on polymer substrates. SnO_2 is more effective in the collection of electrons with low energy compared to TiO_2 resulting in an improved photocurrent in electrochemical cells. Low-energy charge carriers of narrow band-gap perovskite absorbers which contain tin metal or formamidium in their structure might not be efficiently collected by TiO_2 or ZnO but be collected by SnO_2. Therefore, research regarding SnO_2 as an ETM will provide important information in the development of PSCs [75].

2.6.1. Titanium dioxide (TiO_2)

Titanium dioxide (TiO_2) is a crucial inorganic semiconductor, which has been explored in a range of applications. The synthesis method of TiO_2 affects the conversion efficiency of the solar cells. These synthesis methods include; the sol-gel method, chemical vapour deposition (CVD), hydrothermal method, and flame spray pyrolysis (FSP) [72].

According to Shen *et* al., the best-performing solar cell devices, utilized TiO_2 produced via a hydrothermal autoclaving method. However, this conventional hydrothermal fabrication method is time-consuming and needs complicated processes. As an alternative microwave synthesized TiO_2 can be analyzed, due to its rapid heating to the required temperature and crystallization, resulting in a simpler preparation procedure. Microwave-synthesized TiO_2 offers similar photovoltaic performances to those produced by the hydrothermal process. The reaction time needed for crystallization utilizing hydrothermal autoclaving compared to microwave-assisted heating is significantly decreased from 12 hours to approximately 25

minutes, resulting in crystals with a PCE of 8.2 %, which is amongst the highest ranked for microwave-synthesized TiO_2 [76].

Xiao *et* al. reported a modified two-step *in situ* method to produce micron-level thickness, high-performance perovskite-sensitized nanoporous TiO_2 photoanodes. The *in-situ* method permits an effective transmission and separation of the holes and electrons because of the outstanding contact between the TiO_2 and perovskite. The diffusion length is less than the photoanode of the perovskite for electrons, thereby decreasing the thickness of the photoanode, resulting in an enhancement of photovoltaic performances. PSCs with a photoanode thickness at the micron level indicated a higher cell efficiency of 12.22% without the addition of an HTM to the device [77].

2.6.2. Zinc oxide (ZnO)

Zinc oxide (ZnO) is a metal oxide of interest due to its comparable high electron mobility, energy level, and low-temperature fabrication. ZnO films can be produced through multiple solution- or vacuum-based methods, which allow the mass production at low cost of photovoltaic devices. Solution-processed ZnO-based PSCs have received outstanding performances. However, there are still problems that need attention, which include; residual acetate ligands and/or hydroxyl groups remaining on the ZnO surface, accelerating the chemical deposition of the perovskite thin-film throughout the fabrication process [78].

Solution-processed ZnO nanoparticles have been implemented in the development of multiple thin-film photovoltaic technologies. The ZnO-NPs synthesized can be processed without additional annealing treatment at room temperature. Cheng *et* al. speculate that there are disadvantages to using ZnO as the ETM in PSCs that only short annealing time and low annealing temperature can be used, limiting the photovoltaic performance and the perovskite crystal growth [79].

The probability of ZnO compact layer deposition allows the suitability of acquiring the compact layer at low temperatures. Amid the multiple techniques that can be used to produce the ZnO layer, the superior method seems to be chemical deposition. Semiconductors produced via chemical deposition illustrate better charge transfer properties in comparison to alternative methods, such as electrodeposition. The ZnO compact layer, which is in agreement with solution-based PSC fabrication procedures, can be produced by a low-temperature chemical deposition procedure [80].

Liu and Kelly illustrated that ZnO colloidal nanoparticles that are spin-coated can be used as the ETL in perovskite devices, resulting in a PCE of 15.7 % [81]. However, most ZnO growth

methods that have been reported, involve harmful chemical reagents, which include polymeric coatings that might serve as impurities, elevated temperature systems, and sophisticated and expensive equipment. Therefore, the challenge is the development of an inexpensive, energy-efficient, and environmentally friendly technique to synthesize ZnO NPs that is amicable for the sustainable production of PSCs on a large scale. Pelicano *et* al. establish that the simple oxidation of zinc in water could fabricate high-quality ZnO NPs that may be used not only for future photovoltaics but can be used in other ZnO-based electronics [82].

2.6.3. Tin dioxide (SnO_2)

Tin dioxide (SnO_2) is one of the most favorable alternatives to conventional metal oxides, such as TiO_2, in PSCs due to its larger bandgap and higher electronic mobility, indicating outstanding long-term stability and a swifter transport of the photogenerated electrons [83].

There are multiple methods of SnO_2 synthesis available, namely, pulsed laser deposition, co-precipitation, polymeric precursor method, solid-state synthesis, sol-gel, and spray pyrolysis approaches. The sol-gel method is one of the best methods used for thin-film preparation of high quality, based on the polycondensation and hydrolysis of metal alkoxides [84].

According to Matsui *et* al., SnO_2 exhibits perovskite materials and well-placed conduction bands of SnO_2 in the planar configuration, which is crucial in fabricating PSCs with a highly stabilized power output. SnO_2 electron selective layers produced via the solution-processing procedure produce highly efficient PSCs with a PCE of approximately 21%. However, films produced by chemical bath deposition result in blocking layers that have a high selectivity which supports the highest voltages of 1214 mV with a bandgap of 1.62 eV [85]. Figure 2.13. below, illustrates the bandgap difference between ZnO and SnO_2. SnO_2 has a wider bandgap than ZnO, with higher electron mobility and low processing temperatures [85].

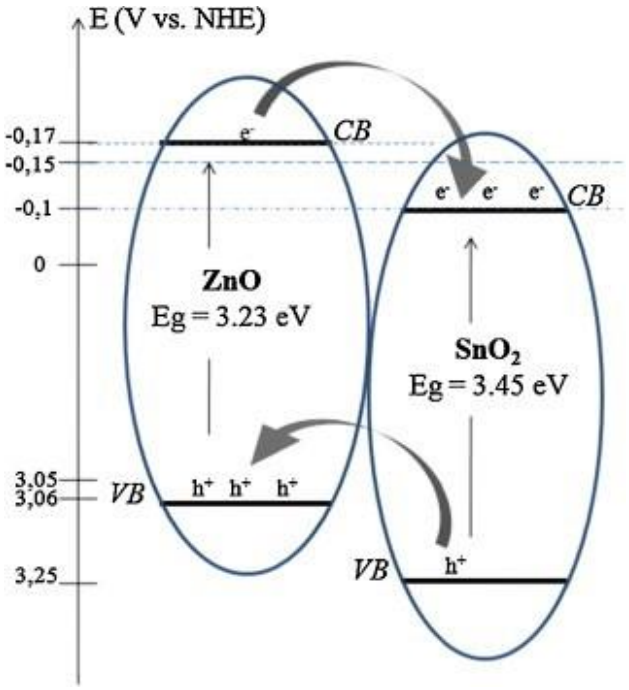

Figure 2.13: Diagram illustrating the bandgap difference between ZnO and SnO_2

Table 2.3 displays the different performance parameters of materials used in the ETL. TiO_2, in comparison to ZnO and SnO_2, displayed the highest FF, whereas ZnO displayed the highest J_{sc}, V_{oc}, and PCE. The PCE of ZnO can be attributed to it having a higher short-circuit density (J_{sc}) of 21.60 $mA.cm^{-2}$ and open-circuit voltage (V_{oc}) of 1.04 V in comparison to that of TiO_2 and SnO_2 [74].

Table 2.3: Summary of ETMs performance parameters

HTM	**Parameters**				
	FF (%)	J_{SC} ($mA.cm^{-2}$)	V_{OC} (V)	PCE (%)	References
TiO_2	73.77	13.89	0.761	7.80	[86]
ZnO	63.4	21.60	1.04	14.24	[78]
SnO_2	41.8	18.8	0.647	5.12	[74]

CHAPTER THREE

Materials and Methods

This chapter consists of a list of materials used in this project, along with the synthesis, and characterization of the materials. The parameters used for the fabrication of the PSCs are detailed within the chapter, as well as a brief description of the characterization techniques and the instruments used.

3.1. Materials

All chemicals that were used in this investigation are presented in table 3.1. These chemicals were used to synthesize $MAPbI_3$, $MAPbBr_3$, rGO, ZnO and SnO_2 as discussed in the following section and subsections.

Table 3.1: Materials, Supplier, and purity of materials used throughout the project

Chemical Name	Chemical formula	Supplier	Purity
Lead iodide	PbI_2	Sigma Aldrich	99.999 %
Dimethylfomamide	$(CH_3)_2NCH$	Sigma Aldrich	99.999%
Methylammonium iodide	CH_3NH_3I	Sigma Aldrich	99.99%
2-propanol	$(CH_3)_2CHOH$	Sigma Aldrich	99.5%
Lead bromide	$PbBr_2$	Sigma Aldrich	99.999%
Methylammonium bromide	CH_3NH_3Br	Sigma Aldrich	≥99%
Dimethyl sulfoxide	$(CH_3)_2SO$	Sigma Aldrich	≥99.9%
Sulfuric acid	H_2SO_4	Sigma Aldrich	99.999%
Graphite	C	Sigma Aldrich	≥99.99%
Sodium nitrate	$NaNO_3$	Sigma Aldrich	≥99.0%
Potassium permanganate	$KMnO_4$	Sigma Aldrich	≥99.0%
Hydrogen peroxide	H_2O_2	Sigma Aldrich	≥30%
Hydrochloric acid	HCl	Sigma Aldrich	37%
Zinc acetate dihydrate	$Zn(CH_3COO)_2 . 2H_2O$	Sigma Aldrich	99.999%
Methanol	CH_3OH	Sigma Aldrich	≥99.8%
Potassium hydroxide	KOH	Sigma Aldrich	≥85%
Chloroform	$CHCl_3$	Sigma Aldrich	≥99.8%
n-butanol	$CH_3(CH_2)_3OH$	Sigma Aldrich	≥99.4%
Acetone	CH_3COCH_3	Sigma Aldrich	≥99.5%
Ethanol	CH_3CH_2OH	Sigma Aldrich	99.8%
Spiro-OMeTAD	$C_{81}H_{68}N_4O_8$	Sigma Aldrich	99%
Bis(trifiuoromethane)sulfonimide (LiTFSI)	$C_2F_6LiNO_4S_2$	Sigma Aldrich	99.95%
Chlorobenzene	C_6H_5Cl	Sigma Aldrich	99.8%
Acetonitrile	CH_3CN	Sigma Aldrich	99.5%
4-tert-butylpyridine	$C_9H_{13}N$	Sigma Aldrich	96%
Terephthalic acid	$C_6H_4(CO_2H)_2$	Sigma Aldrich	98%
Tin chloride dihydrate	$SnCl_2 . 2H_2O$	Sigma Aldrich	98%
Silver powder	Ag	Sigma Aldrich	99.99%

3.2. Methylammonium Lead Triiodide ($MAPbI_3$)

3.2.1. Solution processing

The $MAPbI_3$ solution was synthesized by dissolving 461 mg of PbI_2 (Sigma, Aldrich 99.999% trace metals basis, perovskite grade) in a 1 ml mixture of Terephthalic acid (TPA, 8 mg/ml) and DMF (Dimethylformamide $(CH_3)_2NCH$). The solution was stirred on a hot plate for 4 hours at 70 °C [38] until the solute completely dissolved, which formed a transparent yellow solution containing PbI_2 crystals [91, 92]. A solution of methylammonium iodide (MAI) and 2-propanol with a concentration of 10 mg/ml was used to make a solution of 25 ml. To make up a 25 ml solution with a concentration of 10 mg/ml, 250 mg of the MAI was weighed and transferred into a 25 ml volumetric flask and made up to the 25 ml mark with the 2-propanol solution. The solution was then filtered using a syringe filter, with a pore size of 0.45 μm [85, 92].

$$PbI_2 + CH_3NH_3I \rightarrow CH_3NH_3PbI_3 \qquad \text{(Rxn 3.1)}$$

3.2.2. Spin-coating process and parameters

The PbI_2 precursor solution was preheated along with the substrates at 70 °C. Once preheated, the first layer was prepared by dropping 60 μl of the PbI_2 solution onto the substrate and spin-coated for 30 seconds at 3000 rpm as illustrated in figure 3.1. The as-coated films were then annealed for 1 hour at 100 °C.

Once the first layer was completed, 60 μl of the MAI/2-propanol solution was dropped onto the substrates and allowed to penetrate the PbI_2 layer for 40 seconds before being spin-coated. After the MAI/2-propanol solution was allowed to penetrate the PbI_2 layer, the substrate was spin-coated for 30 seconds at 2000 rpm and annealed for 20 minutes at 70 °C.

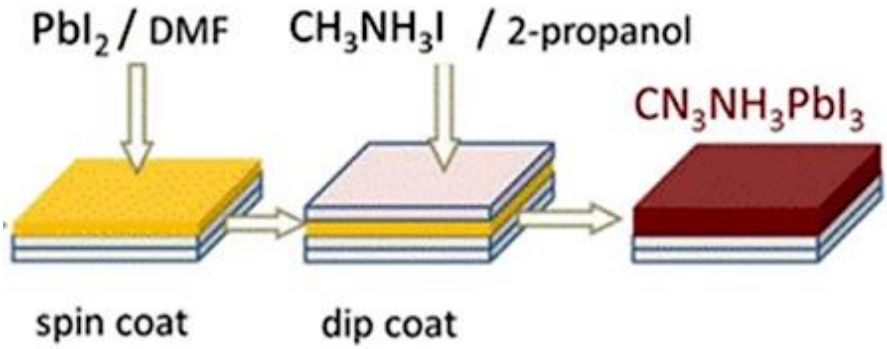

Figure 3.1: Schematic illustration of the spin-coating process for $MAPbI_3$ formation

3.3. Methylammonium Lead Tribromide ($MAPbBr_3$)

3.3.1. Solution processing

The $MAPbBr_3$ solution was synthesized by dissolving 361 mg of $PbBr_2$ (Sigma, Aldrich 99.999% trace metals basis, perovskite grade) in 1 ml of DMF and stirred at 70 °C for 3 hours until the solute dissolved [89]. The second layer's solution was prepared by dissolving 0.2 g of MABr in 10 ml of 2-propanol (IPA) [89]. The solution prepared was filtered using a syringe filter, with a pore size of 0.45 μm [35].

$$PbBr_2 + CH_3NH_3Br \rightarrow CH_3NH_3PbBr_3 \qquad \text{(Rxn 3.2)}$$

3.3.2. Spin-coating process and parameters

The $MAPbBr_3$ layer required the solution preparation. The first step required 60 µl of the $PbBr_2$/DMF solution, which was dropped onto the ETL and spin-coated at 4000 rpm for 15 s as illustrated in figure 3.2. The layer was subsequently annealed at 70 °C for 15 minutes. The second step was performed by dropping 60 µl of the MABr/IPA solution onto the first layer and allowing it to penetrate the $PbBr_2$ layer. Once the second layer was allowed to penetrate the first, the solution was spin-coated at 3000 rpm for 5 s and annealed at 70 °C for 30 minutes. [89]

Figure 3.2: Schematic illustration of the spin-coating process for $MAPbBr_3$ formation

3.4. Reduced Graphene Oxide (rGO)

3.4.1. Synthesis

Graphene oxide was synthesized using a modified Hummers' method [90]. Sulphuric acid (40 ml) was added to graphite powder (500 mg) and stirred, before the addition of sodium nitrate (375 mg). The mixture was stirred inside a cool beaker for 2 hours, while potassium permanganate (3 g) was slowly added. The mixture was then stirred for an additional 4 hours and was allowed to reach room temperature before it was heated for 30 minutes at 35 °C. Once

heated, deionized water (50 ml) was poured into the flask and the solution was stirred for an additional 15 minutes at 70 °C. Once completed, an additional 250 ml of deionized water was added while the unreacted potassium permanganate was removed with the addition of hydrogen peroxide (2-10 ml). The resulting solution was filtered and washed with 1 M hydrochloric acid and deionized water before being oven-dried [90]. The graphene oxide mechanism is displayed in figure 3.3.

The prepared graphene oxide was reduced by placing the graphene oxide (50 mg) into a crucible. The crucible containing the graphene oxide was placed in a furnace for 4 hours at 200 °C to remove oxygen-containing functional groups. The resulting reduced graphene oxide was allowed to cool to room temperature [59].

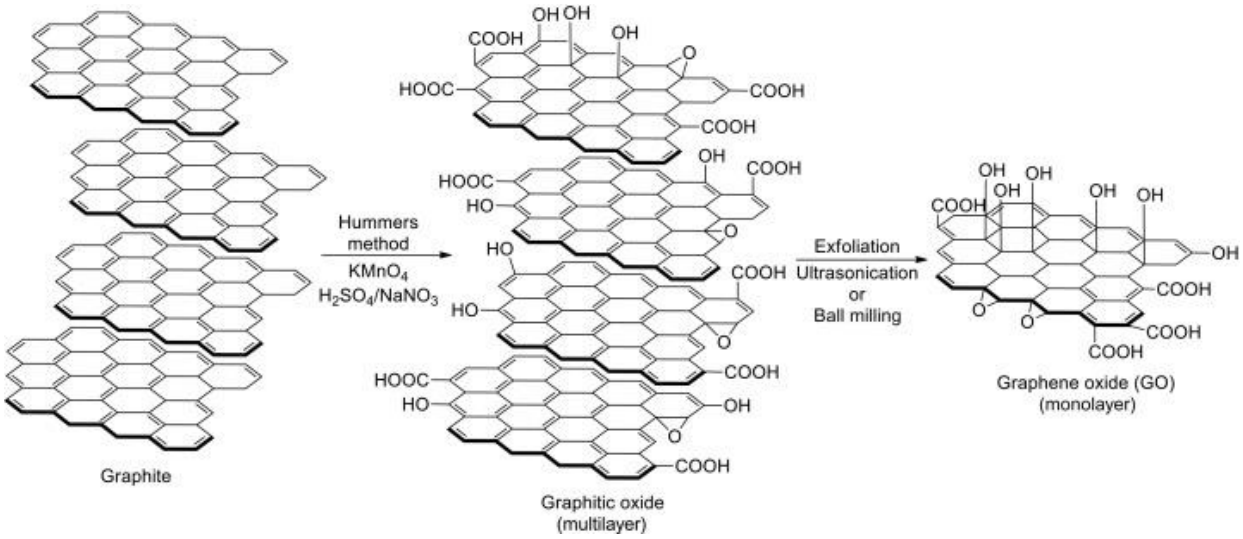

Figure 3.3: Graphene oxide formation mechanism

3.4.2. Spin-coating process and parameters

rGO dispersion was made by dispersing the rGO in 2-propanol at a concentration of 0.6 mg/ml and sonicated for 1 hour.

The rGO dispersion was spin-coated over the perovskite photo-active layer for 60 seconds at 5000 rpm [65]. The substrates were annealed for 10 minutes at 120 °C [91].

3.5. Zinc Oxide (ZnO)

3.5.1. Synthesis

ZnO was synthesized by employing the sol-gel process. Zinc acetate dihydrate (2.95 g, 13.4 mmol) was dissolved in methanol (125 ml) while being stirred at approximately 65 °C. A

solution containing potassium hydroxide (KOH) (1.48 g, 23 mmol) in methanol (65 ml) was added dropwise over a 15 min period at 60-65 °C. The mixture was stirred at 65 °C for 2.5 hours while covered with parafilm. The mixture was then cooled down to room temperature, the contents poured into centrifuge vials and the supernatant decanted. The precipitate was washed thrice with methanol (5 ml) and centrifuged for 5 minutes. A solution containing methanol (5 ml), chloroform (5 ml), and n-butanol (70 ml) was made, and the solution (10 ml) was added to each vial. This solution was used to disperse the precipitate, producing a ZnO nanoparticle solution. The ZnO nanoparticle solution was filtered using filter paper and filtered once more using a syringe filter [81].

$$Zn(CH_3CO_2)_2.2H_2O + KOH \rightarrow Zn(OH)_2 + C_2H_3O_2K \rightarrow ZnO + H_2O \qquad \text{(Rxn 3.3)}$$

3.5.2. Spin-coating process and parameters

Prior spin-coating ZnO, the filtered solution obtained at the end of the synthesis was sonicated for 5 minutes. This solution was then used for the spin coating process.

Approximately 100-200 μL of the sample was placed onto the substrate and spin-coated for 30 seconds at 3000 rpm. This was then repeated 2 times, before being allowed to dry in the fume hood for 2 minutes to form the ZnO layer [88].

3.6. Tin dioxide (SnO_2)

3.6.1. Synthesis

For the synthesis of SnO_2, 8.374 g of $SnCl_2.2H_2O$ was dissolved in 100 ml of absolute ethanol. The mixture was stirred and refluxed at 80 °C for 3 hours. Subsequently, the mixture was allowed to cool down to room temperature under continuous stirring for an additional hour.[92]

$$SnCl_2.2H_2O + C_2H_5OH \rightarrow Sn(OCH_2CH_2OH)_2 \rightarrow SnO_2 \qquad \text{(Rxn 3.4)}$$

3.6.2. Spin-coating process and parameters

The solution acquired from the synthesis was aged overnight, resulting in the SnO_2 organic sol which was used for coating [93].

The SnO_2 film was deposited onto the ITO-glass substrate by spin-coating the above dispersion for 30 seconds at 3000 rpm and annealed for 30 minutes at 150 °C [71].

3.7. Spiro-OMeTAD

3.7.1. Solution processing

The solution was prepared by dissolving 180 mg of Spiro-OMeTAD in 1 ml of chlorobenzene along with 37.5 µl of LiTFSI (170 mg/ml) in acetonitrile and 17.5 µl of 4-tert-butylpyridine [35].

3.7.2. Spin-coating process and parameters

The Spiro-OMeTAD was deposited onto the perovskite photoactive layer by spin-coating for 20 seconds at 4000 rpm and allowed to dry overnight.

For the fabrication of the cells, the materials were spin-coated, following the process illustrated in ***Fig. 3.4***. The process requires the application of the solvent solutions onto the pedestal, the pedestal was rotated causing the dispersion of the solution onto the desired surface; it was then allowed to dry before being repeated to form the layers of the cell [69].

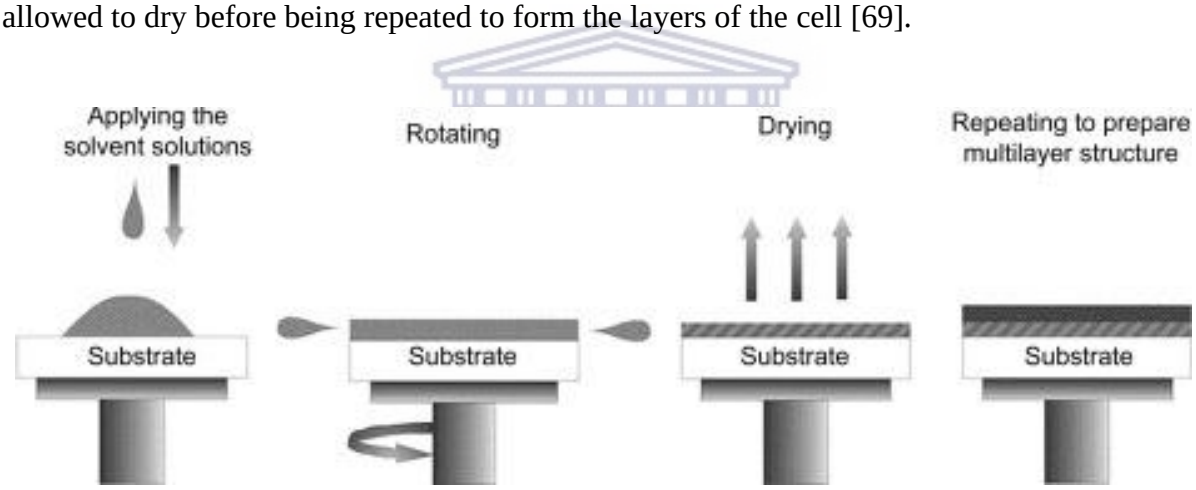

Figure 3.4: An illustration of the overview of the spin coating process

However, before fabrication of the cells ITO substrate was subjected to a cleaning process as described below:

Substrate cleaning

I. The ITO coated glass was ultrasonically cleaned using detergent, deionized water, acetone, and ethanol, sequentially for 15 minutes.
II. Once cleaned, the substrate was removed using a pair of tweezers and dried under nitrogen flow.
III. After the use of the nitrogen flow, it was additionally dried by placing the ITO-coated glass in the oven for 2 hours at 120 °C [91].

The structures of cells generally have a planar device or inverted device structure. In planar device architecture, the electron transporting layer (ETL) (e.g. SnO_2 and ZnO) is spin-coated onto a glass substrate followed by the perovskite photoactive layer (e.g. $MAPbI_3$ and $MAPbBr_3$), hole-transporting material (HTM) (e.g. rGO and Spiro-OMeTAD) and a metal contact (e.g. gold) as depicted in *Figure 3.5a and b*, whereas, in the inverted device architecture, the ETL and HTM are switched around, as shown in *Figure 3.5c and d* [94].

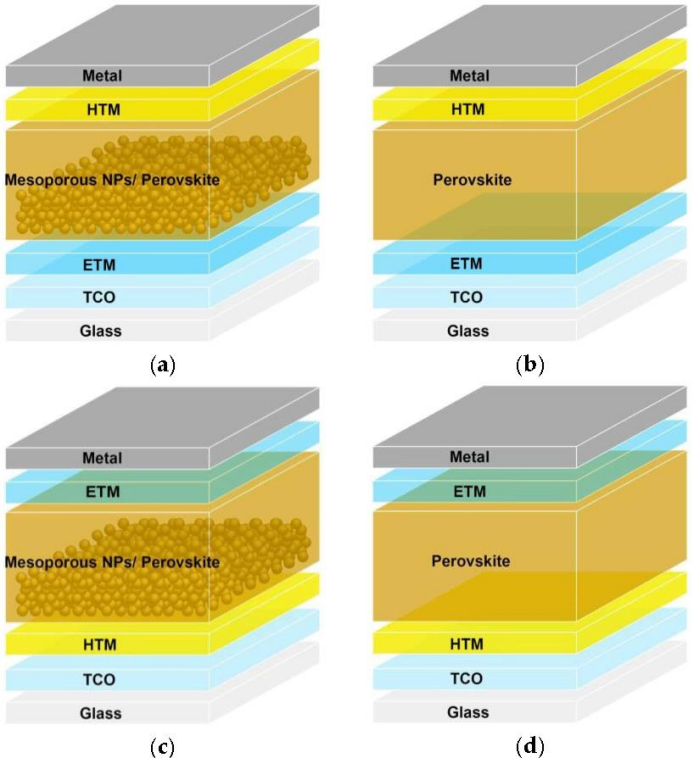

Figure 3.5: Schematic illustrations of common PSC device architectures, namely: a) n-i-p mesoporous, b) n-i-p planar, c) inverted p-i-n mesoporous, and d) inverted p-i-n planar structures

There are several possible ways in which to construct the cell based on the materials synthesized. These possibilities are constructed to determine the best combination of materials to use to assemble an efficient and stable cell. Comparisons are made with regards to the ETL, HTMs, and perovskite photoactive layer, resulting in 8 different cell fabrications, as mentioned below:

The following structures will be fabricated, namely;

i) glass/ ITO/ SnO_2/ $MAPbI_3$/ rGO/ Ag,

ii) glass/ ITO/ SnO_2/ $MAPbI_3$/ Spiro-OMeTAD/ Ag,

iii) glass/ ITO/ ZnO/ $MAPbI_3$/ rGO/ Ag,

iv) glass/ ITO/ ZnO/ $MAPbI_3$/ Spiro-OMeTAD/ Ag,

v) glass/ ITO/ SnO_2/ $MAPbBr_3$/ rGO/ Ag,

vi) glass/ ITO/ SnO_2/ $MAPbBr_3$/ Spiro-OMeTAD/ Ag,

vii) glass/ ITO/ ZnO/ $MAPbBr_3$/ rGO/ Ag and

viii) glass/ ITO/ ZnO/ $MAPbBr_3$/ Spiro-OMeTAD/ Ag.

Figure 3.6. shows a typical illustration of the device architecture aimed for. The 8 device fabrications previously mentioned will be following this type of architecture and the best combination of materials will be determined.

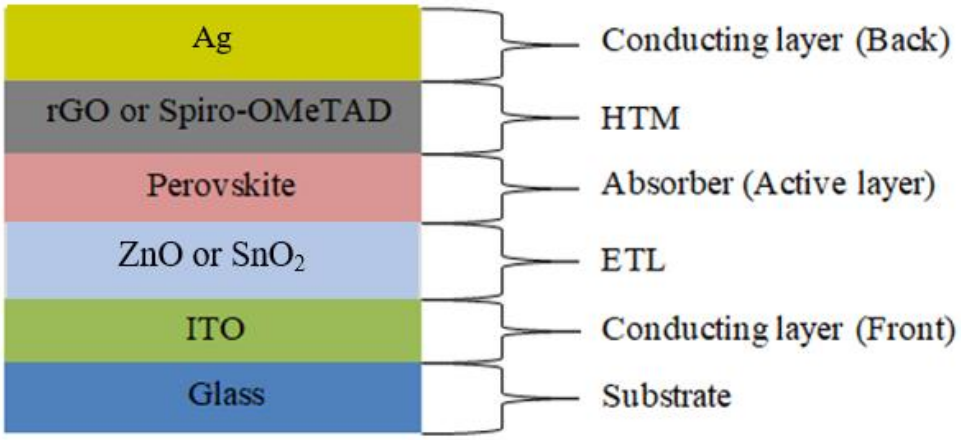

Figure 3.6: Illustration of the device architecture

Figure 3.7 illustrates a complete cell structure along with its corresponding energy band diagram, for $MAPbI_3$-based solar cells with Spiro-OMeTAD as the HTM, which is similar to the device architecture aimed for in this study [35].

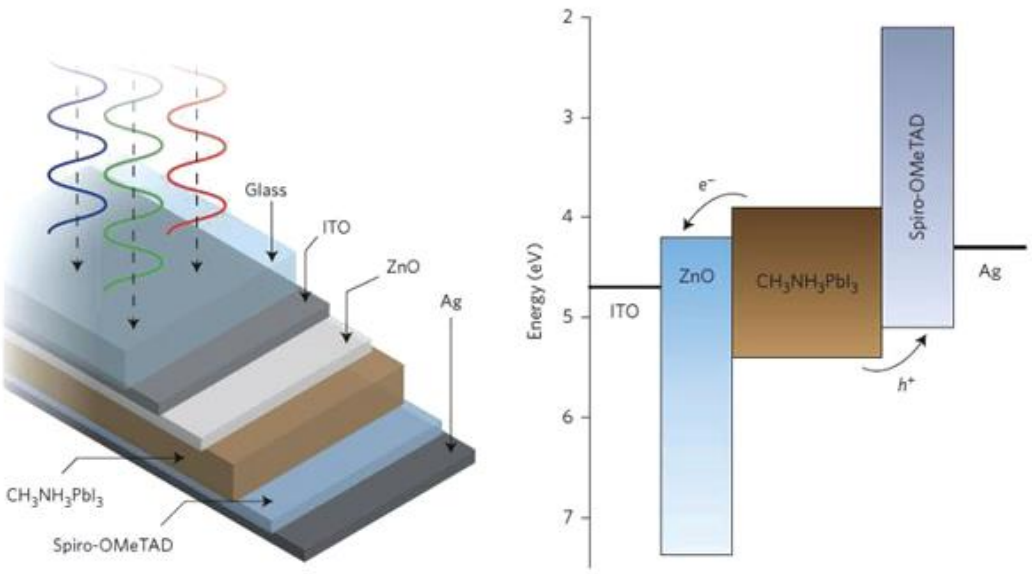

Figure 3.7: The schematic illustration of a complete cell structure (left) with the corresponding energy band diagram (right)

3.8. Characterization Methods

3.8.1. High-Resolution Scanning Electron Microscope (HRSEM)

The morphology and particle sizes of $MAPbI_3$, $MAPbBr_3$, SnO_2, ZnO, and rGO, were analyzed using HRSEM images. The samples were prepared by spin-coating and annealing the materials onto individual ITO coated glass substrates. The images were obtained using the ZEISS ULTRA and MIRA3 TESCAN microscopes with an acceleration voltage of 5.0 kV.

3.8.2. X-Ray Photoelectron Spectroscopy (XPS)

XPS is a method used to analyze the surface chemistry of a material by measuring its elemental composition and the electronic and chemical state of the atoms within the material. A PHI 5000 Scanning ESCA Microprobe with Al-Kα radiation was used for analysis, with a photon energy of hν = 1486.6 eV.

3.8.3. Fourier Transform Infrared (FTIR) Spectroscopy

The structural differentiation and the determination of functional groups of the materials were evaluated using FTIR. The data was obtained using a Thermo Fisher Nexus 670 FTIR spectrometer equipped with an attenuated total reflection (ATR) attachment. The samples were prepared by coating the materials onto ITO-coated glass substrates and placed underneath the ATR attachment.

3.8.4. UV-Visible Spectroscopy (UV-vis)

UV-visible spectroscopy is a quantitative method used to determine the absorption ability of the materials. The materials, $MAPbI_3$, $MAPbBr_3$, SnO_2, ZnO, and rGO, were coated onto the ITO-coated glass substrates and analyzed using Thermo Fisher Scientific's UV-Visible Double Beam Spectrophotometer.

3.8.5. X-ray Diffraction (XRD)

XRD was performed to obtain information regarding the crystalline structure and phase composition of the synthesized materials. A BRUKER AXS X-ray diffractometer with Cu-Kα radiation was utilized for analysis, with a radiation wavelength of $\lambda = 1.54051$.

3.8.6. Cyclic Voltammetry (CV)

Cyclic voltammetry was used to evaluate the electronic behaviour of the synthesized materials. The analysis was performed using a PalmSens potentiostat, employing a three-electrode system, consisting of a working electrode, counter electrode, and reference electrode. For this project, $MAPbI_3$, $MAPbBr_3$, SnO_2, ZnO, and rGO were coated onto an ITO-coated glass substrate and acted as the working electrodes, a platinum wire was used as a counter electrode, and an Ag/AgCl reference electrode in 3M KCl.

3.8.7. Electrochemical Impedance Spectroscopy (EIS)

The electrochemical properties of the materials were determined using EIS. The analysis was performed on the CHI706E Electrochemical Workstation, employing the same three-electrode system used in the CV analysis.

3.8.8. Photoluminescence (PL)

The optical properties of the materials were analyzed using photoluminescence. The materials, which were coated on ITO-coated glass substrates were analyzed using the HORIBA Jobin Yvon NanoLog.

CHAPTER FOUR

Results and Discussion

The following chapter consists of results and a discussion section detailing the outcomes of the characterization techniques. The characterization techniques, include, HRSEM, XRD, FTIR, XPS, UV-vis, PL, CV, EIS, and J-V curves. The degradation of the perovskites and the application of the PSCs are discussed.

4.1. Interface Characterization

4.1.1. Surface morphology

4.1.1.1. High-Resolution Scanning Electron Microscope (HR-SEM)

The surface morphology of the $MAPbI_3$, $MAPbBr_3$, SnO_2, ZnO, and rGO thin films were analyzed using HR-SEM. Figure 4.1(a-e) illustrates the HR-SEM images of $MAPbI_3$, $MAPbBr_3$, SnO_2, ZnO, and rGO thin films, respectively, which were prepared on ITO substrates using the spin-coating deposition method.

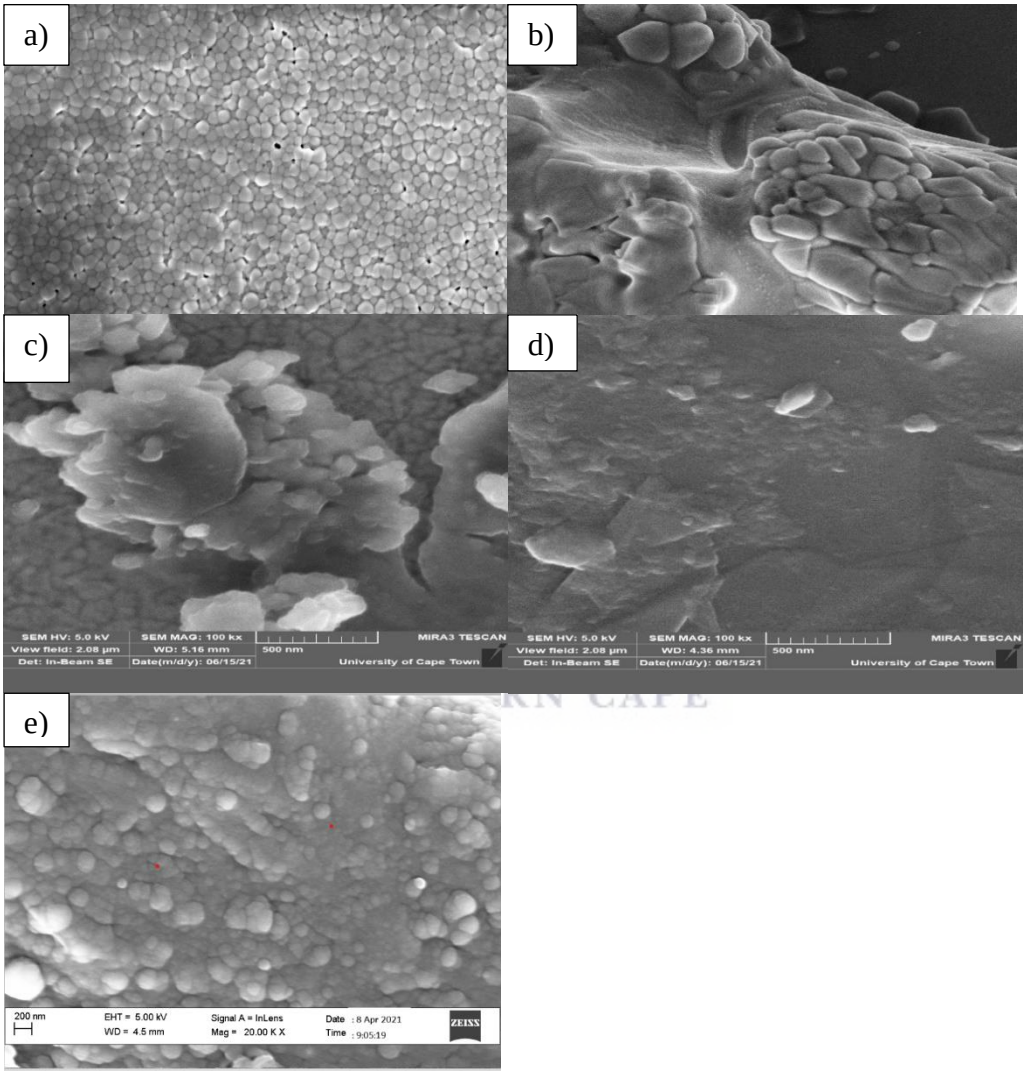

Figure 4.1: The HR-SEM images of a) $MAPbI_3$, b) $MAPbBr_3$, c) SnO_2, d) ZnO and e) rGO

Figures 4.1 (a) and (b) show the perovskite or absorbing layers, namely, $MAPbI_3$ and $MAPbBr_3$ films. $MAPbI_3$ film in figure 4.1(a) depicts a uniform, densely packed layer with good surface coverage. The $MAPbI_3$ grain sizes were relatively large (~268-320nm), however, according to a study performed by Ahmadian-Yazdi *et* al., $MAPbI_3$ film synthesized using DMF generally have grain sizes averaging between ~100 – 650 nm [95]. In comparison to the other perovskite

layer illustrated in figure 4.1(b), $MAPbBr_3$ film shows a relatively rough and densely packed surface without any pinholes, resulting in proper coverage over the entire surface. The surface defects observed in the $MAPbBr_3$ film can cause leakage and consequently increase the dark current, affecting the device performance [96]. The $MAPbBr_3$ grain sizes (~300-420 nm) were larger than that of $MAPbI_3$. According to McGovern *et* al., $MAPbBr_3$ grain sizes average between ~200-500 nm [31]. Grain size controls the formation of grain boundaries in such a way that small grain sizes lead to great grain boundaries. Since grain boundaries facilitate the ion migration pathway, ion migration is easier in film with small grain sizes [97]. Consequently, $MAPbI_3$ film is expected to display better device performance in comparison to $MAPbBr_3$ film. The thickness measurements for these layers were performed using the Veeco Dektak 6M Stylus Profiler (USA), in which the average layer thickness of $MAPbI_3$ was found to be 352 nm and $MAPbBr_3$ film displayed a layer thickness of 373 nm. According to Guan *et* al., the ideal thickness for the absorbing layer using halide perovskites is in the range of 350 – 500 nm [98].

Figures 4.1(c) and (d) show images of the electron transport layer materials, namely, SnO_2 and ZnO films respectively. Figure 4.1(c) illustrates that SnO_2 formed a uniform layer. However, clusters of the SnO_2 particles appear on the uniform layer. These clusters can be a result of the rough surface of the ITO substrate, due to small irregular ITO grains which can lead to less perovskite coverage [71]. The SnO_2 displayed grain sizes in the range of 245-380 nm with a layer thickness of approximately 29.8 nm. The ideal layer thickness of SnO_2 film ranges from 20 – 100 nm. The smaller grain formation increases surface roughness, subsequently, according to Xiong *et* al., SnO_2 nanoparticles agglomerate and increase in size as film thickness increases. Therefore, SnO_2 cannot block holes leading to poor device performance. However, the problem can be solved with the use of a thin ETL as presented [96], [97]. In comparison, figure 4.1(d) illustrates that ZnO film had formed multiple layers on the ITO surface as the ZnO sheets can be seen. Subsequently, the layers cover the entire surface of the ITO, displaying grain sizes of ~143 nm with a layer thickness of approximately 57.4 nm. The ideal layer thickness for ZnO film is in the range of 40 – 100 nm, therefore, the prepared layer fell between the required range. The layer thickness was obtained by forming two layers and could be altered by increasing the number of layers.

Figure 4.1(e) illustrates the HTM, rGO film. The rGO particles can be seen on the surface of the ITO, with grain sizes of ~240 nm and a layer thickness of approximately 39.3 nm. The ideal thickness for the HTL using rGO is in the range of 20 – 60 nm [99].

4.1.2. Phase Composition

4.1.2.1. X-Ray Diffraction (XRD)

The information regarding the crystalline structure and phase composition of the synthesized materials were analyzed using X-ray diffraction (XRD). The results obtained by XRD analysis were filtered with the crystal-impact software, known as MATCH, to remove excess noise and the crystal structures from these results were constructed using the 3D visualization software, known as VESTA. The XRD patterns of the absorbing layer materials, $MAPbI_3$ and $MAPbBr_3$, are displayed in figures 4.2(a) and (c), respectively.

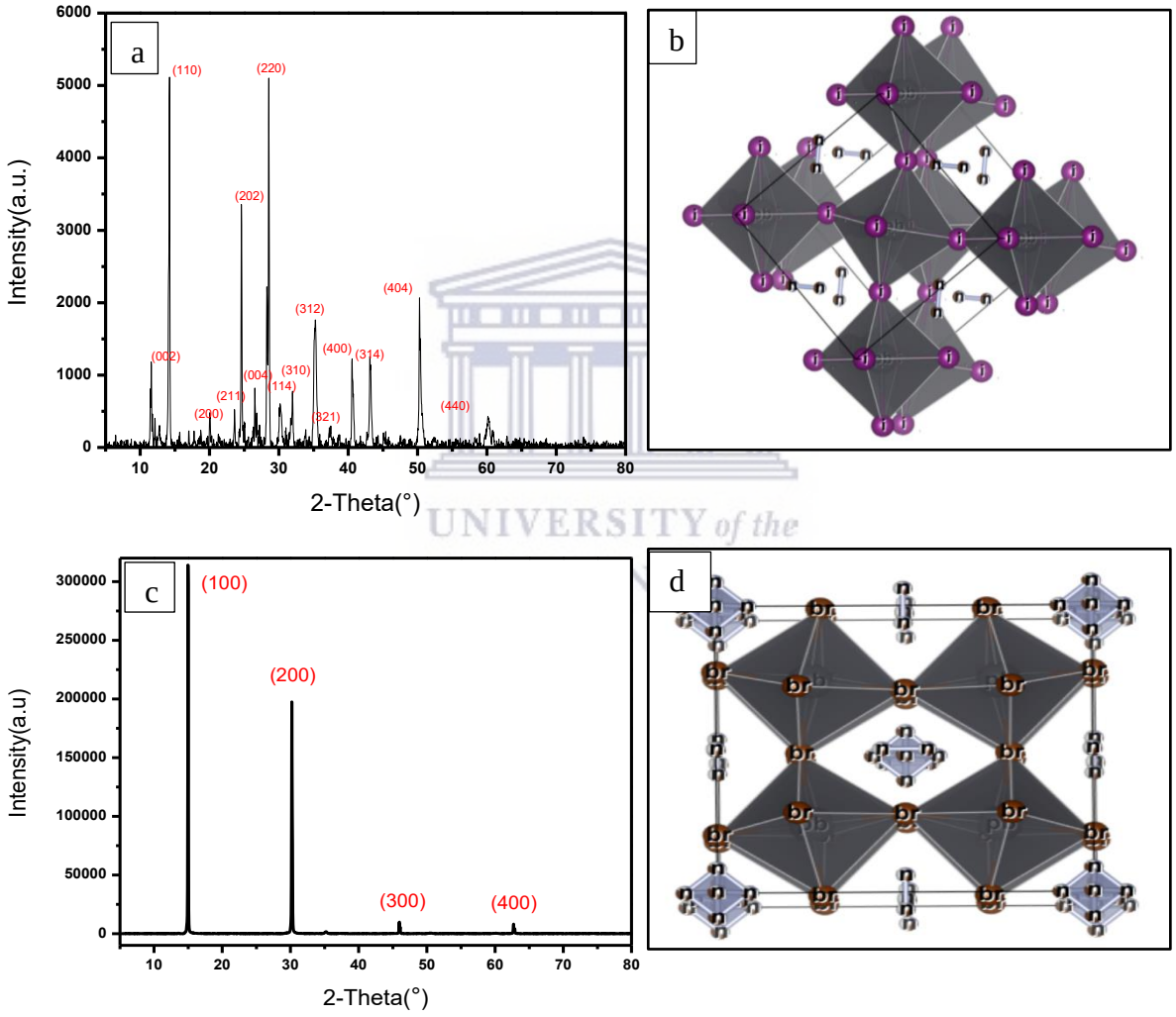

Figure 4.2: XRD patterns of a) $MAPbI_3$ with the corresponding b) $MAPbI_3$ crystal structure and c) $MAPbBr_3$ with corresponding d) $MAPbBr_3$ crystal structure

The XRD pattern displayed in figure 4.2(a), shows peaks at $2\theta = 14.78^{o}$, 28.51^{o}, and 31.98° for $MAPbI_3$ perovskite films that can be indexed to (110), (220), and (310) diffraction of

perovskite grains respectively, which agree with the values of ICSD ID 241477. The peak which occurs at 2θ = 14.78° is attributed to residual PbI_2, which can be beneficial to the photovoltaic performance by improving the carrier lifetime by contributing to the reduction in recombination at the absorber electron selective surface interface [100]. Figure 4.2(b) shows the tetragonal crystal structure obtained from the XRD patterns displayed in figure 4.2(a). The corresponding crystal size for $MAPbI_3$ was calculated to be 97.59 nm. This was calculated using the Debye-Scherrer equation [101]:

$$d = \frac{0.9\lambda}{\beta \cos\theta} \qquad \text{(Eq. 4.1)}$$

where d = d-spacing or crystal size, 0.9 is the value of the shape factor, λ = the wavelength of the X-ray diffraction, β = full width at half maximum of the peak in radians, and θ = Braggs angle in radians.

In comparison to figure 4.2(c), in which $MAPbBr_3$ displays diffraction peaks at 2θ = 14.9º, 30.2º, 45.9º, and 62.7º which can be indexed to (100), (200), (300), and (400) confirming the formation of the cubic perovskite structure, as illustrated in figure 4.2(d), which agree with the values of the ICSD ID 158306. The peak in the (200) plane, displaying a high intensity, can be attributed to the $PbBr_2$ precursor, indicating that the precursor was in excess. However, the peak in the (100) plane has a higher intensity than the peak in the (200) plane, indicating the formation of $MAPbBr_3$ despite one of the precursors being in excess [4].

The calculated crystal size for $MAPbBr_3$ amounted to 216.67 nm, which is more than double that of $MAPbI_3$.

The XRD patterns of the absorbing layer materials, SnO_2 and ZnO, are displayed in figures 4.3(a) and (c), respectively.

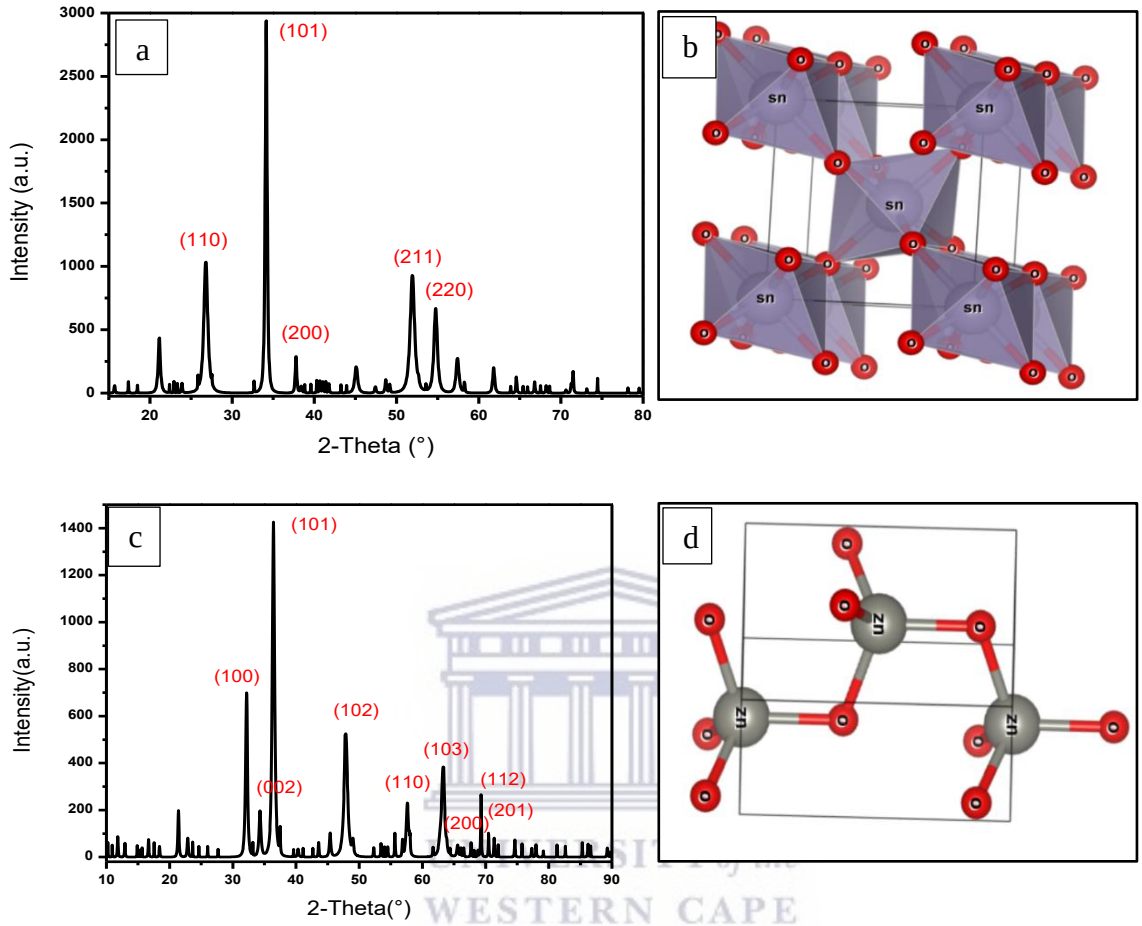

Figure 4.3: XRD patterns of a) SnO_2 with the corresponding b) SnO_2 crystal structure and c) ZnO with corresponding d) ZnO crystal structure

The SnO_2 sample in figure 4.3(a), displays diffraction peaks at $2\theta = 26.8^{o}$, 34.2^{o}, 37.8^{o}, 51.9^{o}, and 57.4^{o}, which corresponds to the (110), (101), (200), (211) and (220) crystal planes, respectively. This shows that the material, as illustrated in figure 4.3(b), has a rutile structure with a tetragonal crystalline system[84] corresponding with ICSD ID 9163. The crystal size for the SnO_2 XRD pattern is determined to be 63.30 nm, which is approximately double that of the grain sizes determined from the SEM results.

ZnO, in figure 4.3(c), displays diffraction peaks at 32.2^{o}, $34.3,^{o}$ 36.4^{o}, and 47.7^{o} which corresponds to (100), (002), (101), and (102) crystal planes of a hexagonal wurtzite crystal structure of ZnO as illustrated in figure 4.3(d), which corresponds to ICSD ID 26170. The crystal size of the ZnO XRD pattern is determined to be 41.52 nm.

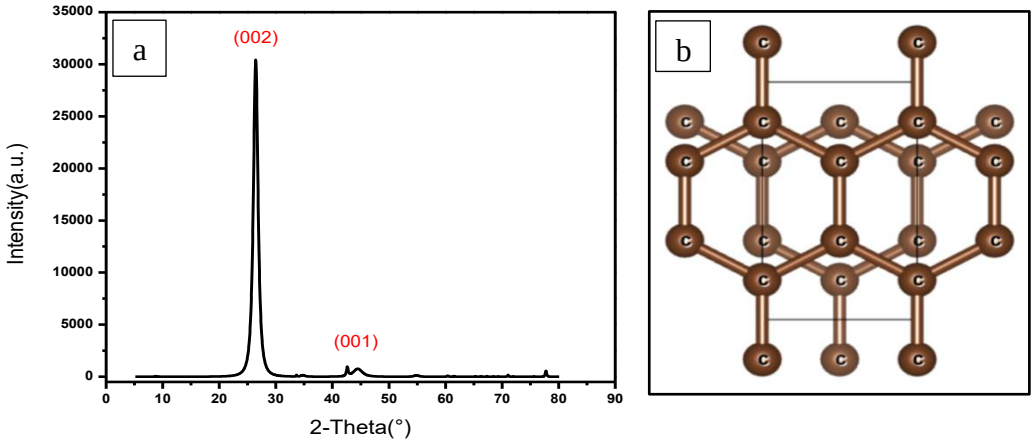

Figure 4.4: XRD patterns of a) rGO with the corresponding b) rGO crystal structure

The XRD pattern of the HTM, rGO, is displayed in figure 4.4(a) with diffraction peaks at 2θ=26.5º and 44.8º, corresponding to the crystal planes (002) and (001), respectively.

This suggests that the rGO sample is well ordered with two-dimensional sheets due to the removal of the functional groups. The d-spacing was calculated to be 17.33 nm.

4.1.3. Elemental Composition

4.1.3.1. Fourier Transform Infrared Spectroscopy (FTIR)

Fourier Transform Infrared Spectroscopy (FTIR) was performed to determine the functional groups present in the prepared materials, namely, $MAPbI_3$, $MAPbBr_3$, SnO_2, ZnO, and rGO thin films.

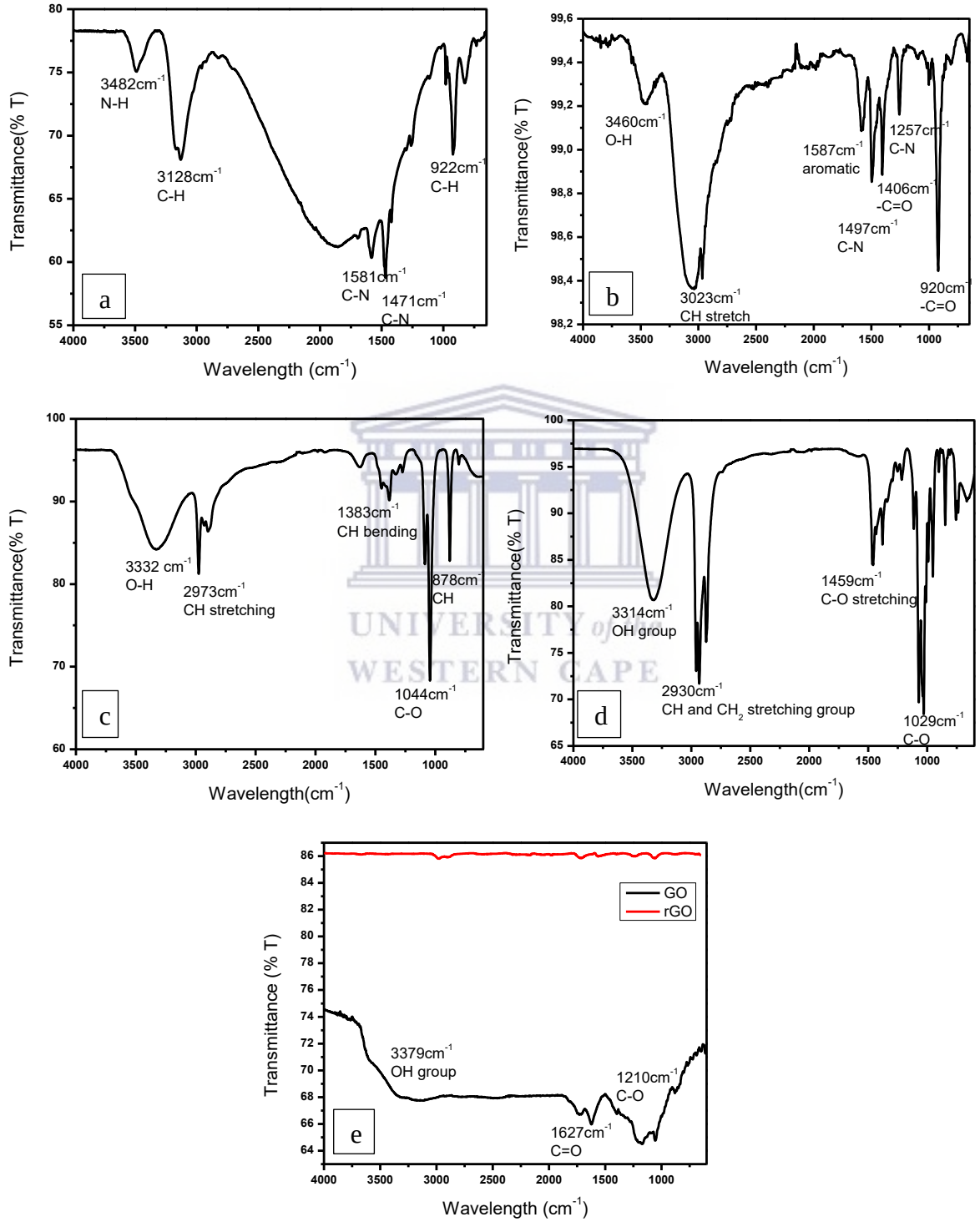

Figure 4.5: The FTIR spectra of a) $MAPbI_3$, b) $MAPbBr_3$, c) SnO_2, d) ZnO and e) rGO thin films on ITO substrates

Figure 4.5(a-e) shows the FTIR spectra of $MAPbI_3$, $MAPbBr_3$, SnO_2, ZnO, and rGO thin films. In figure 4.5(a), there are characteristic vibrational bands of $MAPbI_3$ occurring at 3482 cm^{-1} which is attributed to the N-H stretching vibration, a peak at 3142 cm^{-1} which is attributed to a C-H stretching vibration, a peak at 1581 cm^{-1} which can be attributed to N-H bending and the two remaining peaks positioned at 1471 and 922 cm^{-1} which is attributed to a C-H bending vibration. In comparison to figure 4.5(b) which illustrates vibrational bands of $MAPbBr_3$ at 3460 cm^{-1} which is attributed to O-H stretching vibration, a peak at 3023 cm^{-1} assigned to C-H stretching, and a peak at 1587 cm^{-1} which can be attributed to an aromatic ring. There are two peaks at 1497 and 1257 cm^{-1} which can be attributed to C-N amide bands and an additional two peaks at 1406 and 920 cm^{-1} which can be assigned to a stretching and bending -C=O carbonate, respectively.

Figure 4.5(c) displays the vibrational bands of SnO_2, with characteristic peaks at 3332 cm^{-1} caused by stretching vibrations from OH which could be caused by the absorption of hydroxyl groups of water molecules due to atmospheric moisture[102], with peaks at 2973 and 1383 cm^{-1} occurring due to CH stretching and bending, respectively, for the methyl group coming from the preparation process and a peak 878 cm^{-1} for the vibration bond of Sn-O in SnO_2. In comparison to figure 4.5(d) displaying the vibrational bands of ZnO, the characteristic peak at 3314 cm^{-1} is assigned to the O-H stretching mode of hydroxyl groups, whereas the peak at 2930 cm^{-1} is due to the C-H stretching vibration of alkane groups. The peaks observed at 1459 and 1029 cm^{-1} are due to the asymmetrical and symmetrical stretching of the zinc carboxylate, respectively.

In figure 4.5(e), GO vibrational bands are compared to those of rGO. The characteristic peaks at 2974, 1717, and 1056 cm^{-1} correspond to CH and CH_2 stretching groups, C=O and C-O groups, respectively in the rGO. However, when compared to the GO, it can be noted that the rGO peaks have significantly weakened because of the reduction process.

4.1.3.2. X-Ray Photoelectron Spectroscopy (XPS)

X-ray photoelectron spectroscopy (XPS) was used to measure the materials; $MAPbI_3$, $MAPbBr_3$, SnO_2, ZnO, and rGO, elemental composition as well as the electronic and chemical state of the atoms within these materials to analyze their surface chemistry.

Figure 4.6 (a) and (b) displays the XPS spectra of I 3d5 and Pb 4f, of the material $MAPbI_3$, respectively.

Figure 4.6(a), the I 3d5 peaks with binding energy at 618 and 630 eV for redox state 1-, which corresponds to I 3d5/2 and I 3d3/2, respectively. The separation of 12 eV between the two peaks, can generally be found in the case of I^- species, indicating a well-separated spin-orbit component. The I peak shift towards higher binding energies (blue line), according to Rittisut, suggests that there are small improvements produced in the I^- oxidation state [103].

In figure 4.6(b), the Pb 4f peaks with binding energy 143 and 137.5 eV occur for the 2+ redox state. These can be attributed to the moderate appearance of characteristically signature peaks of PbI_2 and metallic lead (Pb), which corresponds with the XRD results obtained [104]. Consequently, the Pb 4f XPS spectra can be used to detect the decomposition of $MAPbI_3$ due to the reformation of the PbI_2 phase [105]. The decomposition is detected with the shift towards higher binding energies (blue line) in the direction of the precursor PbI_2, which can be caused by the loss of the MAI precursor [106].

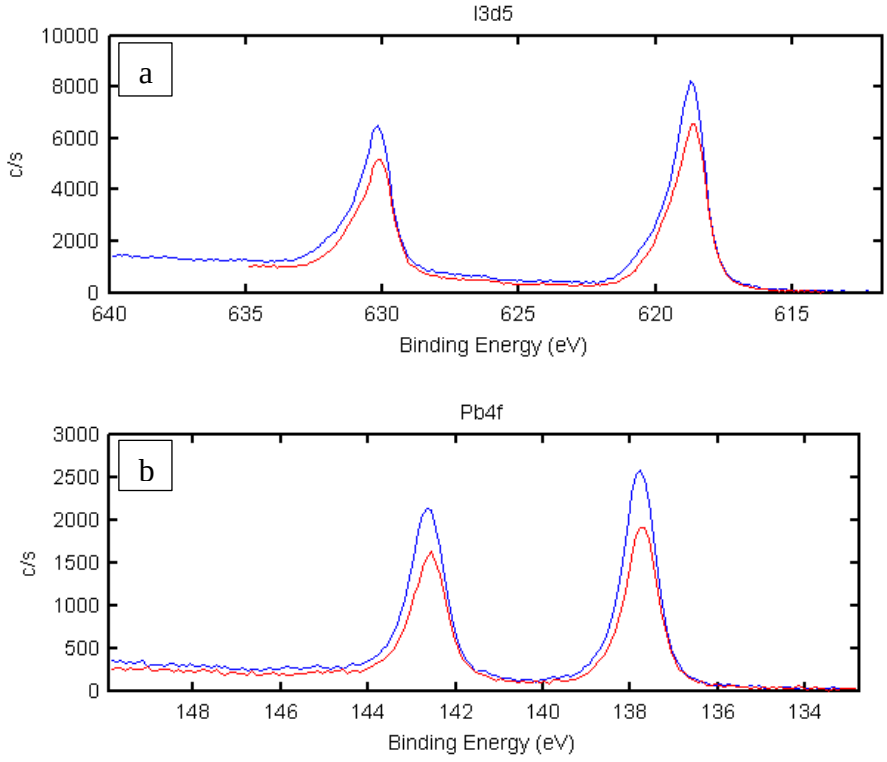

Figure 4.6: The XPS spectra of $MAPbI_3$ a) I 3d5 and b) Pb 4f

Figure 4.7 (a) and (b) above displays the XPS spectra of Br 3d and Pb 4f, of the material $MAPbBr_3$, respectively.

Figure 4.7(a) displays a peak occurring at 68.2 eV with a should occurring at approximately 67 eV for Br 3d because of the surface Br ions. The peaks located in the Br 3d core level with binding energies 68.2 and 67 eV correspond to Br 3d5/2 and Br 3d3/2, respectively [103].

In figure 4.7(b), the two peaks at 137.9 and 142.5 eV for Pb 4f can be attributed to Pb(0) in the metallic state and the perovskite, respectively. According to Wang *et* al., the peaks located in the Pb 4f core level with binding energies 137.9 and 142.5 eV, correspond to the peaks Pb 4f7/2 and Pb 4f5/2, respectively [107].

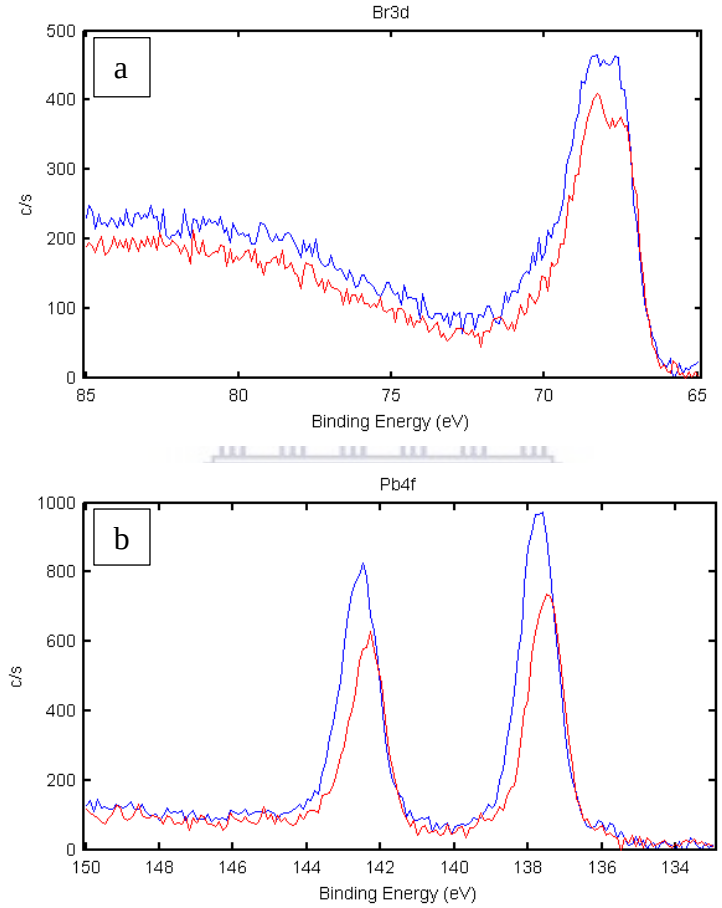

Figure 4.7: XPS spectra of $MAPbBr_3$ a) Br 3d and b) Pb 4f

Figures 4.8(a) and (b), illustrate the Sn 3d and O 1s spectra of the synthesized SnO_2.

In figure 4.8(a) the Sn 3d spectra show binding energies at approximately 487 and 496 eV, which can be assigned to the emission of 3d levels of Sn^{2+} and Sn 4^+ species. According to Xie *et* al., there is a spin-orbit coupling corresponding to the Sn^{4+} valence state, which occurs due to the core level of Sn 3d being spin split into a 3d5/2 and 3d3/2 doublet at the peaks observed above [71].

The O 1s peak observed in figure 4.8(b) is relatively narrow with a binding energy of 531 eV. This peak corresponds to the O^{2-} valence state observed in SnO_2 and oxygen atoms that have been chemisorbed. The peak observed in the O 1s spectra is asymmetrical and has a shoulder located at higher binding energy, which is a result of surface contamination or an irregular morphology of the SnO_2 thin film, which is confirmed by the SEM images. The irregular morphology, according to Akgul *et* al., indicates that the material could contain components that correspond to oxygen atoms bonding in different chemical environments [108].

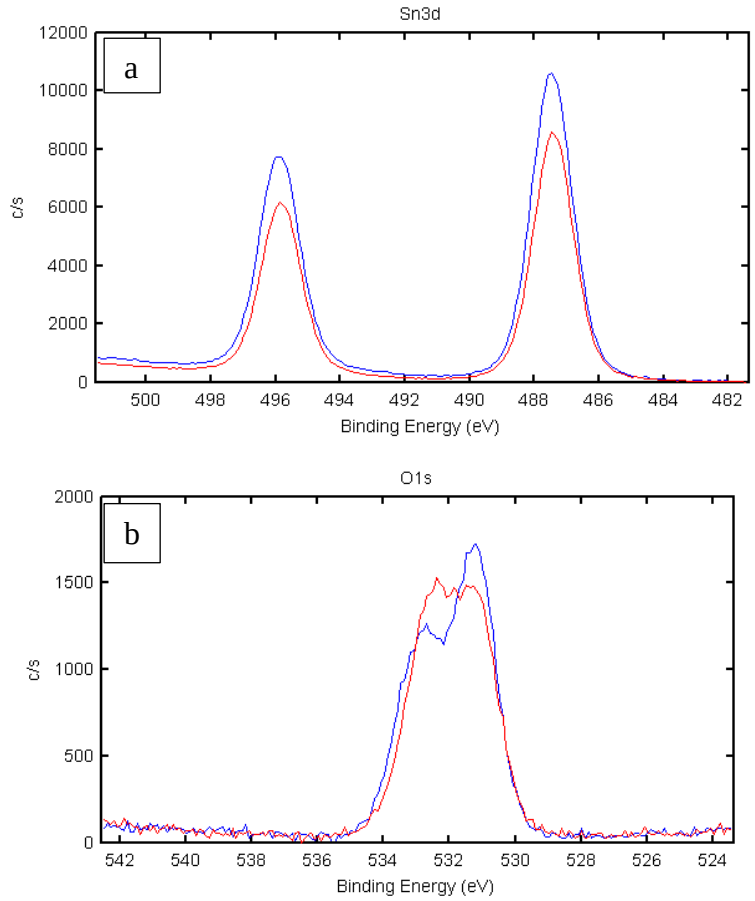

Figure 4.8: XPS spectra of SnO_2 binding energy a) Sn 3d and b) O 1s

The XPS results of ZnO are illustrated in figures 4.9 (a) and (b), showing the spectra of Zn 2p3 and O 1s, respectively. The two peaks displayed in figure 4.9(a), the Zn 2p3 spectrum, with binding energies of 1045 and 1022 eV, can be attributed to Zn 2p1/2 and Zn 2p3/2 of a wurtzite ZnO, which corresponds with the results observed in the XRD patterns of ZnO [78]. The 23 eV difference between the two binding energies suggests that Zn is in a +2 redox state [109]. Figure 4.9(b), displays a peak at 530.3 eV with a shoulder occurring at 531.7 eV, relating to the oxygen atoms, which include oxygen vacancies and surface hydroxyl groups, respectively, in the ZnO structure [78]. According to Chen *et* al, the O 1s spectra are said to have three binding energy components [110]. The peak with the lowest binding energy located at 530.3 eV, can be attributed to the hexagonal wurtzite structure of the Zn^{2+} ion of the metal oxide [111], which is supported by the XRD data obtained. The higher and medium (where the shoulder begins) binding energy components, located at 531.7 and 531 eV, are attributed to an oxygen-deficient region in the ZnO matrix. The asymmetrical nature of the peak observed, according to Das *et* al., reflects the dissimilarity of oxidation numbers of oxygen [112].

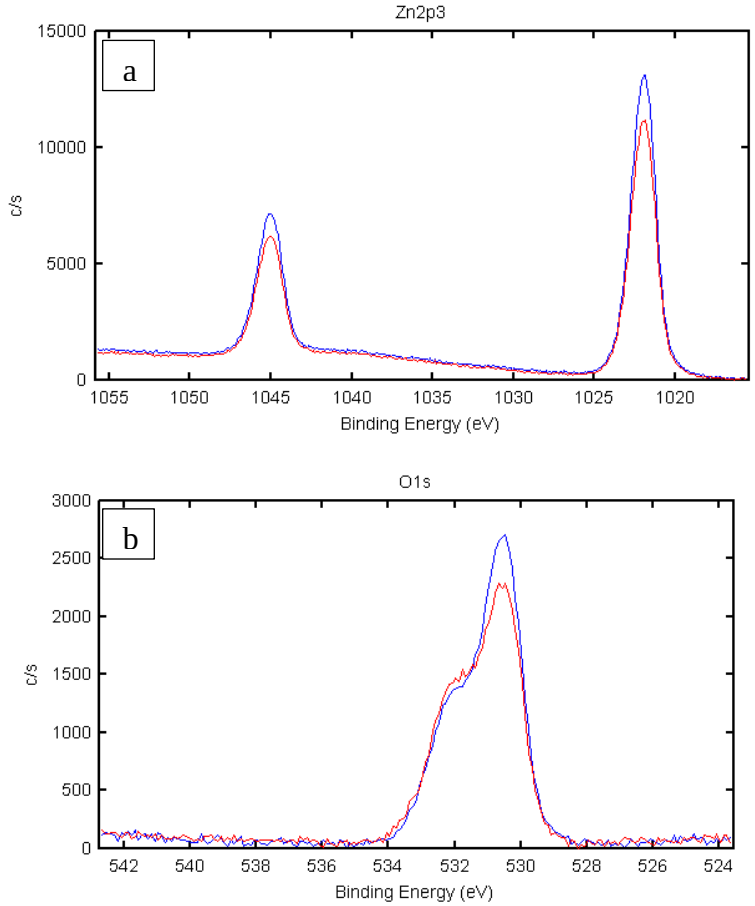

Figure 4.9: XPS spectra of ZnO binding energy a) Zn 2p3 and b) O 1s

The XPS spectra of rGO are displayed in figures 4.10 (a) and (b), displaying its C 1s and O 1s spectra, respectively.

The peak observed in figure 4.10(a) at 284.5 eV corresponds to a C-C stretching in the C 1s spectra. A small tail is observed in the higher binding energy region at 289 eV, which according to Feng *et* al. confirms the restoration of C=C bonds during the reduction of GO to rGO [113]. In figure 4.10(b), the peak observed at 530 eV in the O 1s spectra can be attributed to a quinone group with the shoulder occurring at approximately 531.7 eV, which can be attributed to an oxygen double bonded to a carbon.

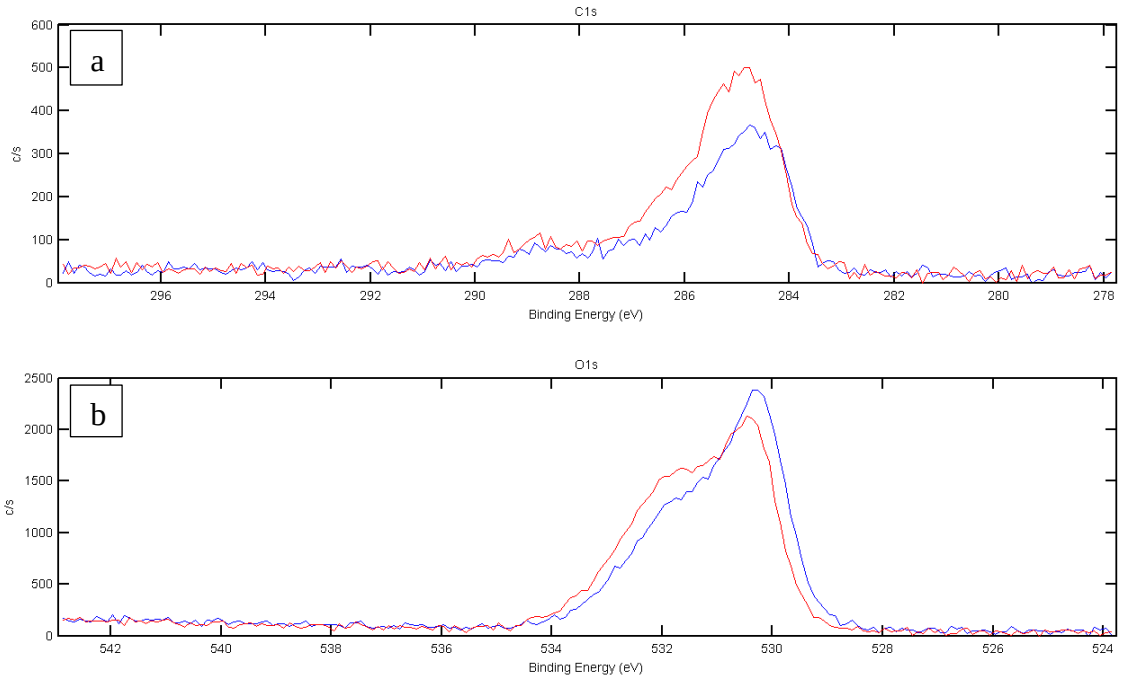

Figure 4.10: XPS spectra of rGO binding energy a) C 1s and b) O 1s

4.1.4. Optical Spectroscopy

4.1.4.1. UV-Visible (UV-Vis) and Photoluminescence (PL) Spectroscopy

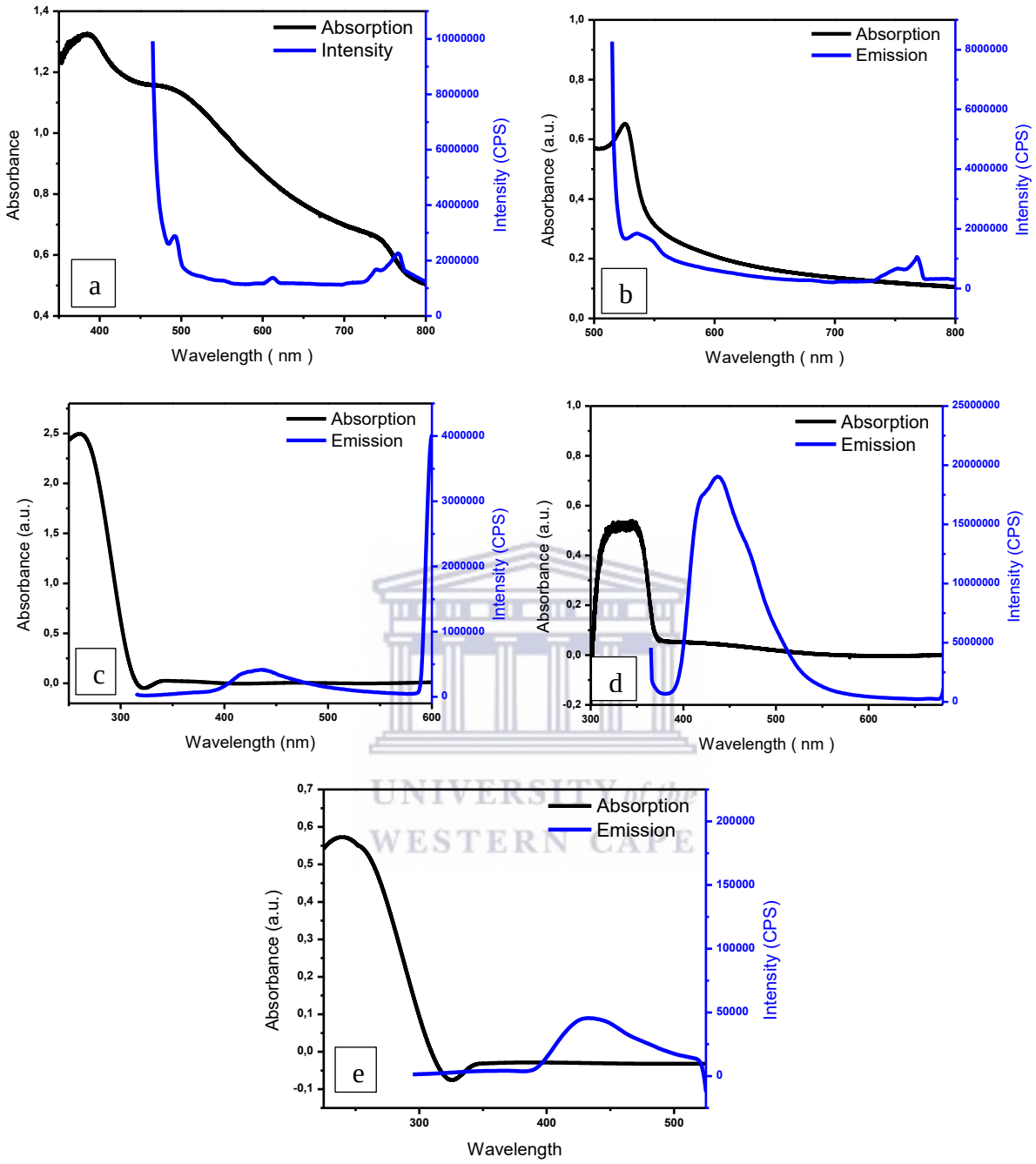

Figure 4.11: The absorption and PL spectra of a) $MAPbI_3$, b) $MAPbBr_3$, c) SnO_2, d) ZnO, and e) rGO thin films on ITO substrates

In figure 4.11(a), the absorption and PL spectra for $MAPbI_3$ are observed. There is an absorbance peak observed at 510 nm which can be caused by excess PbI_2 and a peak at 750 nm which can be attributed to $MAPbI_3$ perovskite formation. Whereas a PL emission peak is observed at 760 nm which is consistent with the perovskite formation of $MAPbI_3$. The peak observed at 475 nm can be attributed to an additional valence band or a charge-transfer state.

In comparison to figure 4.11(b), in which the $MAPbBr_3$ spectra show a clear absorption peak that corresponds to its characteristic absorption limit at 535 nm. The PL spectra of $MAPbBr_3$ show a peak at 538 nm caused by the emission exciton. The peak at 769 nm shows a slight shift towards the longest wavelength relative to the peak of the absorptions.

The absorbance spectra of SnO_2 can be seen in figure 4.11(c), in which a peak can be seen at 260 nm before decreasing to 320 nm where it stabilizes. The PL emission spectra display a band at 430 nm, which according to Marikkannan *et* al., can be attributed to the luminescence centers developed by inertial bonds of tin [114]. The ZnO spectra observed in figure 4.11(d), display a peak at 330 nm which is characteristic of the absorption limit of ZnO, with a PL emission peak observed at 437 nm, which is a blue emission peak originating from the transition of electrons from zinc to the valence band.

In figure 4.11(e), rGO displays an absorption peak at 240 nm before a constant absorbance is observed from approximately 350 nm and above. The peak at 240 nm can be due to the transition of electrons from π-π* of aromatic C-C bonds. Whereas the emission peak observed at 435 nm is a blue emission peak, which is attributed to the recombination of electron-hole pairs localized within small carbon clusters.

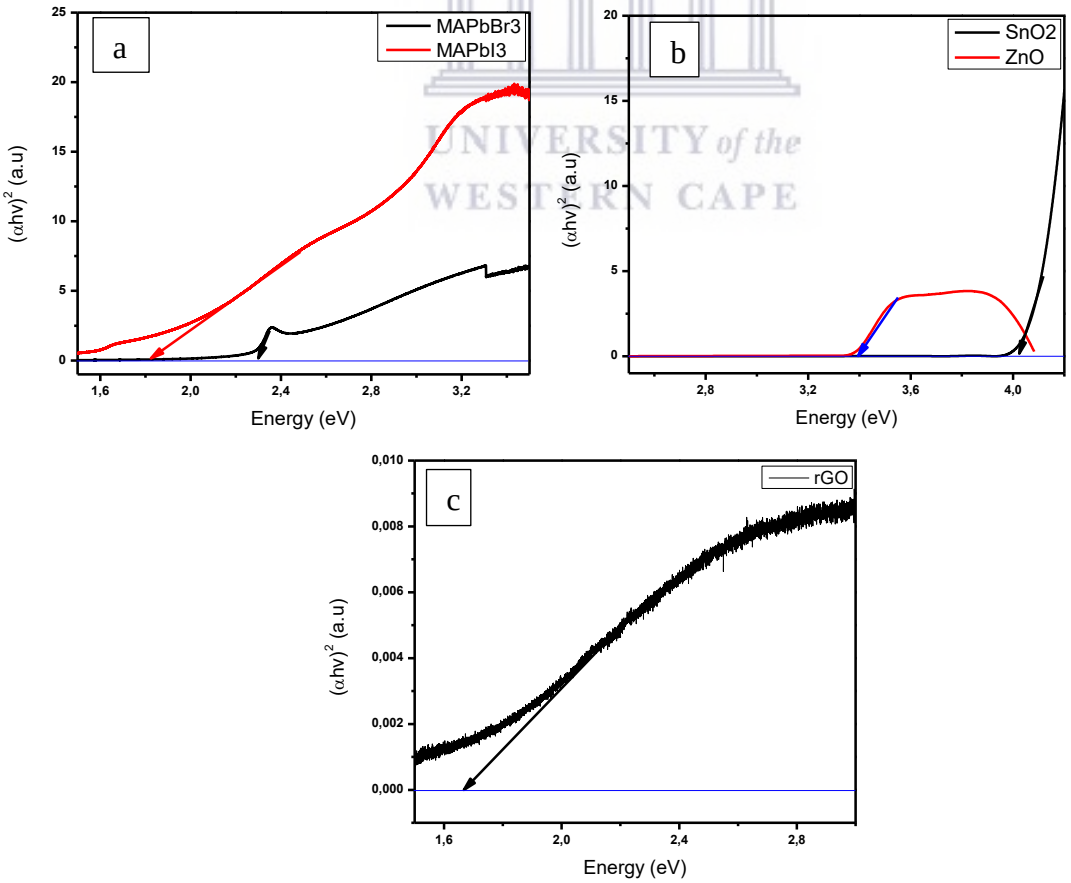

Figure 4.12: Tauc plots for bandgap calculations for a) $MAPbI_3$ and $MAPbBr_3$, b) SnO_2 and ZnO and c) rGO

Perovskites generally have bandgap energies ranging from ~1.55-2.3 eV and in the results obtained in figure 4.12(a), the bandgap energies of $MAPbBr_3$ and $MAPbI_3$, amounted to 2.30 and 1.82 eV, respectively. The range for n-type wide bandgap energy for ZnO ranges ~3.20-3.43 and for SnO_2 ~3.6-4.0 eV, and the bandgap energy calculated, as illustrated in figure 4.12(b) amounted to 3.40 eV and 4.02 eV for ZnO and SnO_2, respectively. The bandgap of SnO_2 being greater than that of ZnO can be related to SnO_2 having larger grain sizes, which is observed in the SEM images.

According to Shen et al., the bandgap energy of rGO is in the range of 1.0 – 1.69 eV depending on the degree of reduction. With the rGO synthesized, the bandgap energy, as illustrated in figure 4.12(c), was 1.67 eV indicating that the GO was reduced. However, the XPS results indicated that there were still functional groups present after reduction [115].

Table 4.1: The bandgap energy values of $MAPbBr_3$, $MAPbI_3$, SnO_2, ZnO and rGO

Sample	Eg (eV)
$MAPbBr_3$	2.30
$MAPbI_3$	1.82
SnO_2	4.02
ZnO	3.40
rGO	1.67

4.1.5. Electrochemistry

4.1.5.1. Cyclic Voltammetry (CV)

The electronic behaviour of the materials was evaluated using cyclic voltammetry, using 0.1 M PBS (pH=7) as an electrolyte. The materials investigated, namely, $MAPbI_3$, $MAPbBr_3$, SnO_2, ZnO, and rGO, were prepared on ITO substrates.

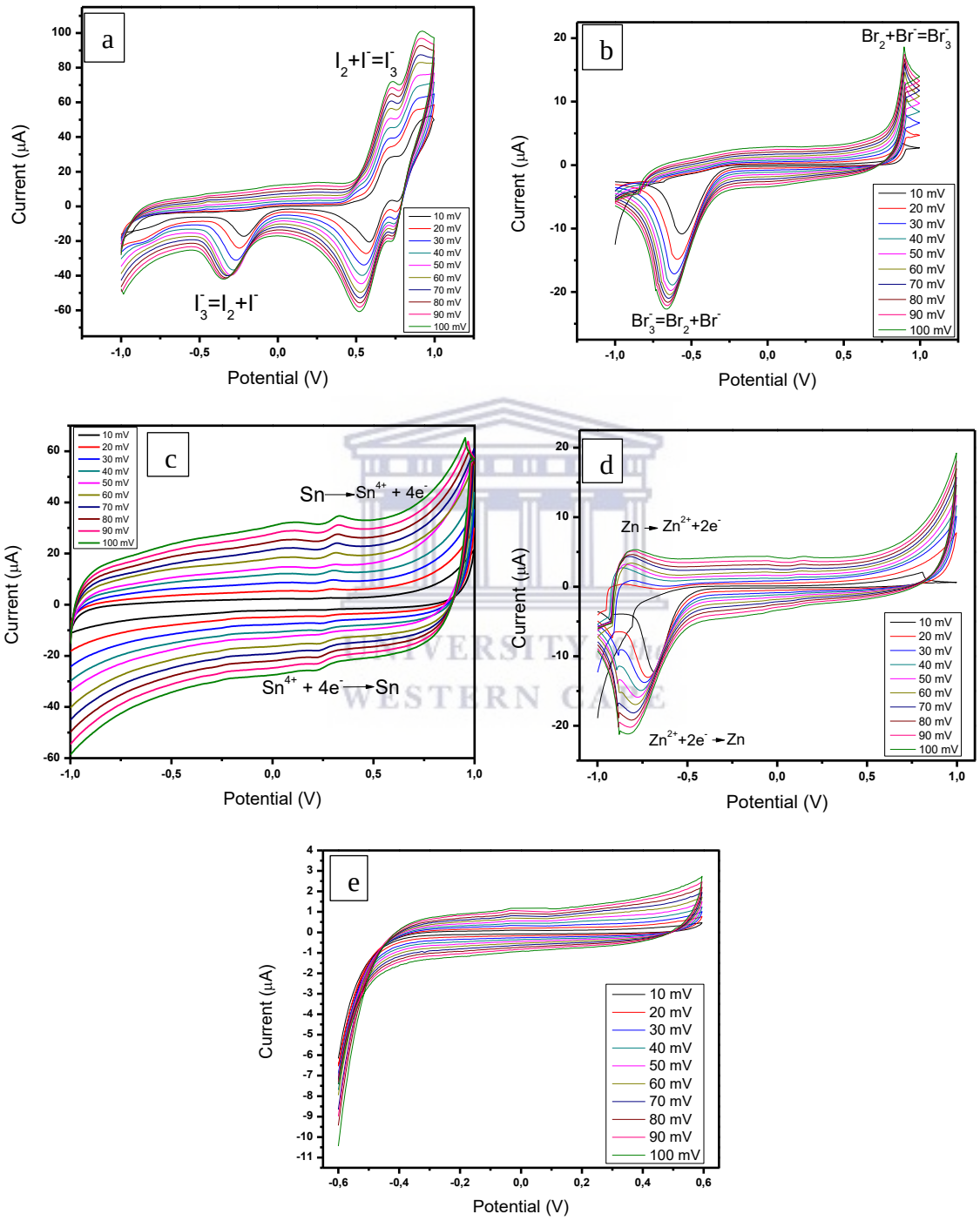

Figure 4.13: Cyclic voltammograms of a) $MAPbI_3$, b) $MAPbBr_3$, c) SnO_2, d) ZnO and e) rGO coated ITO substrates. The analysis was recorded at scan rates of 10 to 100 $mV.s^{-1}$ in 0.1M of PBS (pH=7)

The analysis was performed using a potential window of -1.0 V to +1.0 V for the materials except for rGO, which was investigated in the potential window of -0.6 V to +0.6 V, with scan rates ranging from 10 mV/s to 100 mV/s. A three-electrode system consisting of an ITO coated glass substrate as the working electrode, a platinum wire as the counter electrode, and an Ag/AgCl reference electrode in 3M KCl, was used. In figure 4.13(a), it can be seen that there are two oxidation and two reduction peaks, resulting from the analyses of the spin-coated $MAPbI_3$. The oxidation peaks displayed at 0.8 and 0.92 V can be attributed to the oxidation of the iodide ions and the formation of the perovskite crystal, with the corresponding reduction peaks at 0.53 and -0.35 V because of the reduction of the oxidized perovskite crystal and iodide ions, respectively. Compared to figure 4.13(b), only one oxidation and reduction peak can be seen for $MAPbBr_3$. This oxidation peak observed at 0.9 V corresponds to halide oxidation in lead halides with the corresponding reduction peak observed at -0.66 V. The peak observed for halide oxidation is slightly shifted to the right and the reduction peak is slightly shifted to the left in figure 4.13(b), in comparison to figure 4.13(a). This can be attributed to the weaker solvation of iodide due to its larger size, leading to a larger adsorption enthalpy, in comparison to its bromide counterpart [116].

In figure 4.13(c), small oxidation and reduction peaks are observed for SnO_2 in the range of 0.1 to 0.4 V. The voltammogram shows an oxidation peak at 0.34 V indicated by the oxidation of Sn to Sn^{4+} and a reduction peak at 0.19 V for the reduction back to Sn. The voltammogram illustrated in figure 4.13(d), shows an oxidation peak at -0.8 V indicated by the oxidation of Zn to Zn^{2+} and a reduction peak at -0.83 V for the reduction back to Zn. The oxidation and reduction peaks for ZnO in figure 4.13(d) are shifted to the left in comparison to those displayed by SnO_2 in figure 4.13(c).

Figure 4.13(e) displays the voltammogram of rGO which was conducted from -0.6 to 0.6 V, with no visible peaks, which corresponds to rGO.

4.1.5.2. Electrochemical Impedance Spectroscopy (EIS)

The materials were further electrochemically characterized using EIS in 0.1 M PBS (pH=7). The materials were coated onto the ITO substrate glass, which was once again utilized as the working electrode. The Nyquist and Bode plots of the materials are plotted and discussed below, with the fitted EIS results presented in table 4.3.

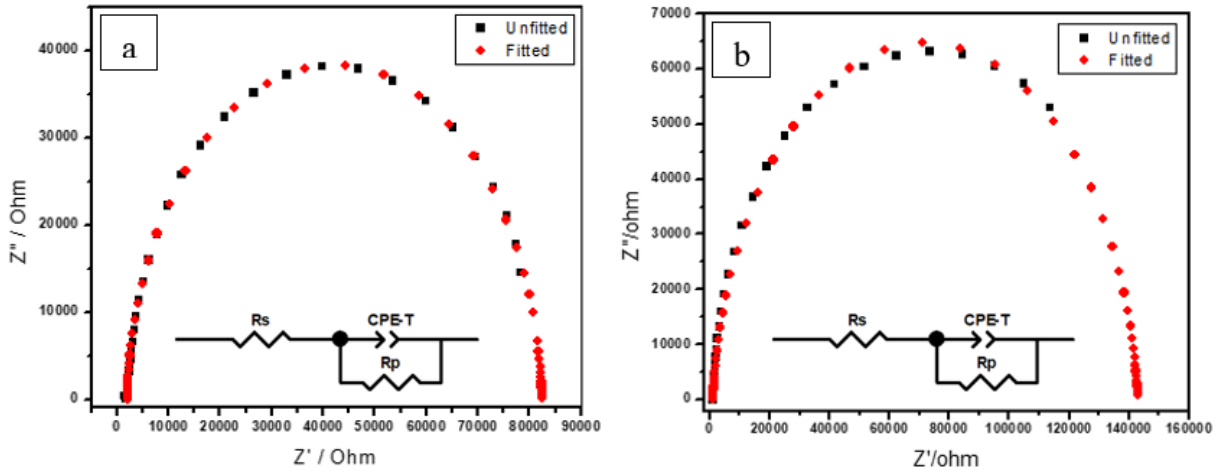

Figure 4.14: The EIS spectra showing the Nyquist plot with its equivalent circuit models of a) $MAPbI_3$ and b) $MAPbBr_3$

The Nyquist plots of $MAPbI_3$ (a) and $MAPbBr_3$ (b) are illustrated in figure 4.14 above.
The EIS results depicted in figure 4.14(a), display a single semicircle that can be attributed to the single-crystal nature of $MAPbI_3$. Due to the appearance of the semicircle and lack of diffusion characteristics, this could indicate that the charge transfer process is kinetically controlled.
The semicircle in the high-frequency region and a straight line in the low-frequency region reflects that the charge transfer process at the conductive matrix interface is observed in figure 4.14(b).

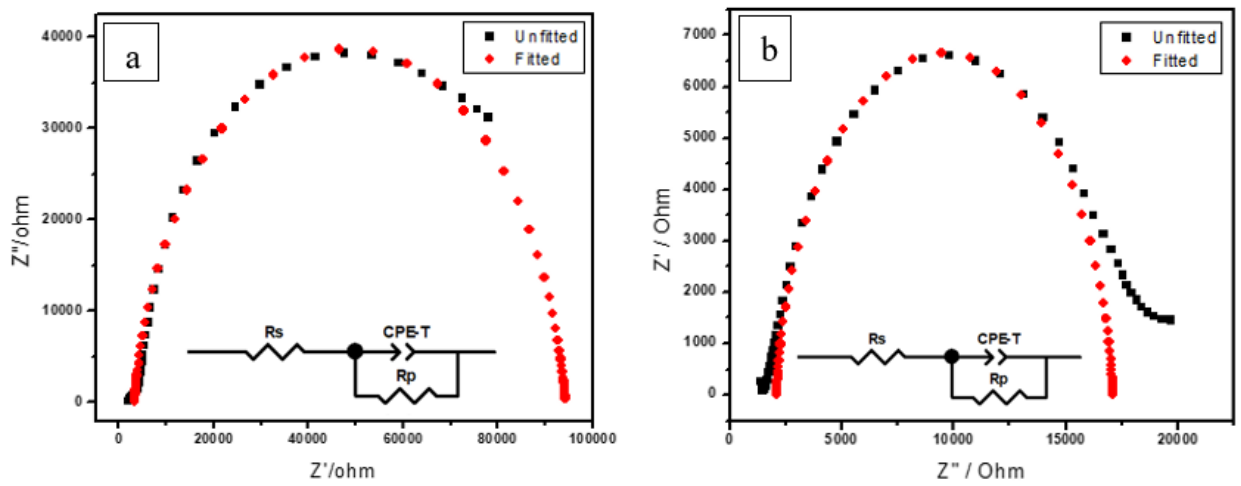

Figure 4.15: The EIS spectra showing the Nyquist plots with the equivalent circuit models of a) SnO_2 and b) ZnO

The spectra displayed in figure 4.15(a), depict a semicircle in which the semicircle in the middle frequency is attributed to the charge transfer resistance.

The plot displayed in figure 4.15(b) depicts an arc, suggesting it is more efficient in interfacial charge transfer. The semi-circle observed in ZnO could be attributed to the grain-to-grain boundaries.

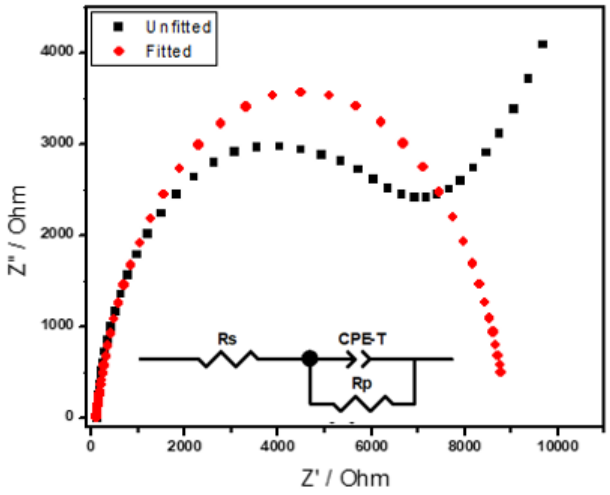

Figure 4.16: The EIS spectra showing the Nyquist plot and its equivalent circuit of rGO

The Nyquist plot, displayed in figure 4.16, corresponds to the charge-transfer resistance-limiting process that is generally associated with rGO. The linearity at the back end of the plot suggests that, due to the diffusion process, has a particularity towards the electrode.

Table 4.2: The EIS fitted results obtained from the circuit and EIS data

Materials	EIS Fitting results			
	R_s	Charge Transfer (R_{ct}) (Ohm)	Max. Frequency (Hz)	Time constant (s)
rGO	116.3	665	38.3	4.16×10^{-3}
$MAPbI_3$	200.5	805	31.6	5.04×10^{-3}
$MAPbBr_3$	110.9	142	17.8	8.94×10^{-3}
SnO_2	325.7	910	2.15	7.40×10^{-2}
ZnO	209.1	151	14.7	1.08×10^{-2}

In table 4.2, the solution resistance (R_s) and charge transfer resistance (R_{ct}) values were obtained from the software Z-View once the EIS data was used to determine its equivalent circuit model and the maximum frequency was determined from the EIS spectra.

The time constant which is an indication of the electron transfer kinetics was calculated using:

$$\tau = \frac{1}{2\pi f_{max}} \quad \text{(Eq. 4.2)}$$

, where an increase in τ relates to blocking of the electrolyte at the interface due to hindrance of insertion/extraction of electrolyte ions. Here, f_{max} is the angular frequency at the maximum impedance [83].

The f_{max} of SnO_2 is 2.15 Hz, compared to the other materials with an f_{max} of 38.8, 31.6, 17.8, and 14.7 Hz for rGO, $MAPbI_3$, $MAPbBr_3$, and ZnO, respectively, which is significantly smaller, indicating that SnO_2 has a longer lifetime and consequently a lower recombination rate [83].

According to the calculations, it can be concluded that $MAPbBr_3$ has the lowest R_{ct}, and SnO_2 has the highest resistance, which should correspond to a fast and slow rate of charge transfer, respectively, due to the blocking rate of electrolyte at the electrode/electrolyte interface evident by a decrease/increase in time constant value (τ). SnO_2 displayed the largest time constant of 7.4×10^{-2} s, indicating the electron transport is much faster compared to the rest of the materials.

Table 4.3: A summary of the materials performance parameters

Materials	HOMO (eV)	LUMO (eV)	Optical Bandgap (eV)	Hole mobility ($cm^2.V^{-1}.s^{-1}$)	Diffusion coefficient ($cm^2.s^{-1}$)
SnO_2	-4.38	-0.36	4.02	2.4×10^{-10}	7.14×10^{-8}
ZnO	-3.45	-0.05	3.40	6.1×10^{-9}	6.88×10^{-7}
$MAPbBr_3$	-5.16	-2.86	2.30	3.11×10^{-7}	8.11×10^{-9}
$MAPbI_3$	-4.88	-3.06	1.82	4.92×10^{-7}	7.39×10^{-8}
rGO	-5	-3.33	1.67	7.43×10^{-9}	1.37×10^{-6}

Table 4.3 displays the HOMO, LUMO, optical bandgap, hole mobility, and diffusion coefficient performance parameters of the materials.

The HOMO and LUMO of the materials were calculated with ferrocene as a reference, using a value of -4.4 eV. The energy levels of the materials were calculated using the following equations:

$$E(HOMO) = -e\,[E_{ox}^{onset} + 4.4\ eV] \qquad \text{(Eq. 4.3)}$$

$$E(LUMO) = E(HOMO) + E_g \qquad \text{(Eq. 4.4)}$$

where E_{ox} is the onset value of the oxidation peak and E_g is the bandgap value.

The hole mobility (μ_p) can be calculated as follows:

$$\boldsymbol{\mu_p} = \frac{d^2}{V\tau_c} \qquad \text{(Eq. 4.5)}$$

where d = sample thickness, V = the applied voltage, and τ_c = time constant.

The hole mobility of the perovskites, with values 3.11×10^{-7} and 4.92×10^{-7} $cm^2.V^{-1}.s^{-1}$ for $MAPbBr_3$ and $MAPbI_3$, respectively, is greater than the HTM, indicating that they are good absorbing layer materials with a fast hole transfer process [74].

The diffusion coefficient is the speed at which a material can diffuse through another material and can be calculated using the Nicholson-Shain equation approach.

$$\boldsymbol{D} = \frac{(i_p^{for})^2 RT}{(0.4463\ n\ c_0 AF)^2 nFv} \qquad \text{(Eq. 4.6)}$$

Where i_p^{for} = the current of the forward peak, R = gas constant (8.314472 $J.mol^{-1}K^{-1}$), T = temperature in Kelvin, n = number of transferred electrons, c_0 = the initial concentration, A = the electrode area, F = Faraday's constant (96485.339 $C.mol^{-1}$) and v = the scan rate used.

Cyclic voltammetry was used to calculate the diffusion coefficients of the materials, while electrochemical impedance spectroscopy was used to calculate the solution and charge transfer

resistances of the materials. The $MAPbI_3$ diffusion coefficient of $7.39x10^{-8}$ $cm^2.s^{-1}$ is approximately nine times greater than its bromide counterpart of $8.11x10^{-9}$ $cm^2.s^{-1}$. This can be caused by the d-spacing in $MAPbI_3$ being two times less than that of $MAPbBr_3$, resulting in a shorter jumping distance between the particles [31]. Similarly, the diffusion coefficient of SnO_2, with a value of $7.14x10^{-8}$ $cm^2.s^{-1}$ is smaller than that of ZnO with a value of $6.88x10^{-7}$ $cm^2.s^{-1}$, which has a smaller d-spacing value than SnO_2. The correlation between the d-spacing value and diffusion is noticed, as the greater the d-spacing value, the smaller the diffusion coefficient. In table 4.3, rGO has the greatest diffusion coefficient, corresponding to the smallest d-spacing value of the materials with a value of 17.3 nm, as calculated from the XRD

4.2. Degradation studies of the perovskites

4.2.1. Methylammonium Lead Triiodide ($MAPbI_3$)

To investigate the effect of aging on $MAPbI_3$, the material without and with TPA was evaluated using UV-visible spectroscopy for three days.

TPA is used to solve the exposed grain boundaries of the thin film, as TPA can act as a template to promote lateral growth of the grains in grain boundaries due to heterogeneous nucleation decreasing the nucleation free-energy barrier found in the grain boundaries [38].

Figure 4.17 illustrates the UV-visible spectra of $MAPbI_3$ without (a) and with (b) TPA. The light absorption intensity for $MAPbI_3$ without (a) TPA is slightly less than that of the $MAPbI_3$ with (b) TPA, however, the light absorption intensity decreased much more significantly in comparison to the perovskite containing the TPA. Subsequently, the enhancement in crystallinity and an increase in grain sizes with the addition of TPA, led to a much more stable perovskite, as the light absorption intensity showed minuscule change over three days, in comparison to the perovskite without the addition of TPA.

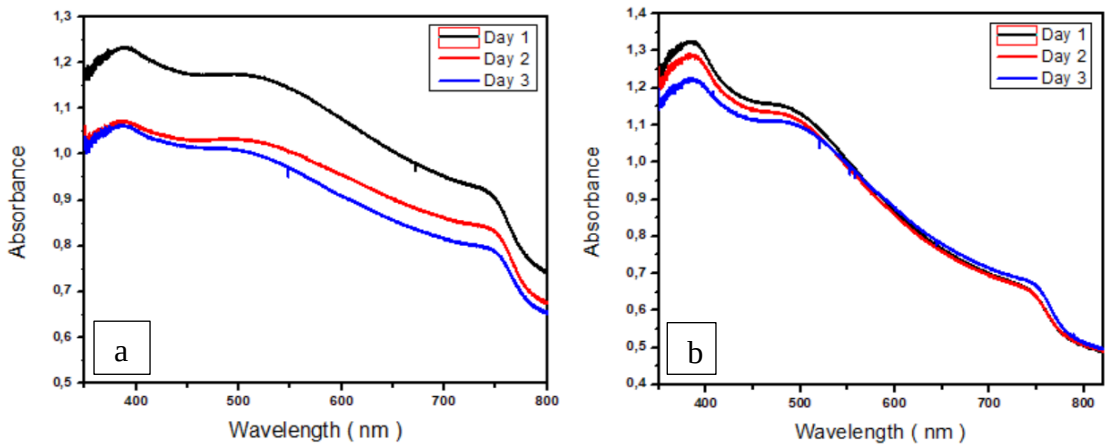

Figure 4.17: UV-Visible spectra of $MAPbI_3$ a) without and b) with terephthalic acid (TPA)

4.2.2. Methylammonium Lead Tribromide ($MAPbBr_3$)

To investigate the effect of aging on $MAPbBr_3$, the material without and with chlorobenzene (CB) was evaluated using UV-visible spectroscopy for three days.

CB is an antisolvent used to increase the performance of perovskite films by promoting heterogeneous nucleation via supersaturation, simultaneously, improving the stability of PSCs.

Figure 4.18 illustrates the UV-visible spectra of $MAPbBr_3$ without (a) and with (b) CB, in which both spectra show a decrease in absorbance over three days. However, (b) shows a significant increase in light absorption, in comparison to (a). This is due to the enhancement in crystal quality and perovskite film thickness caused by the addition of CB to the spin-coating process to maximize the supersaturation of the perovskite precursor [117].

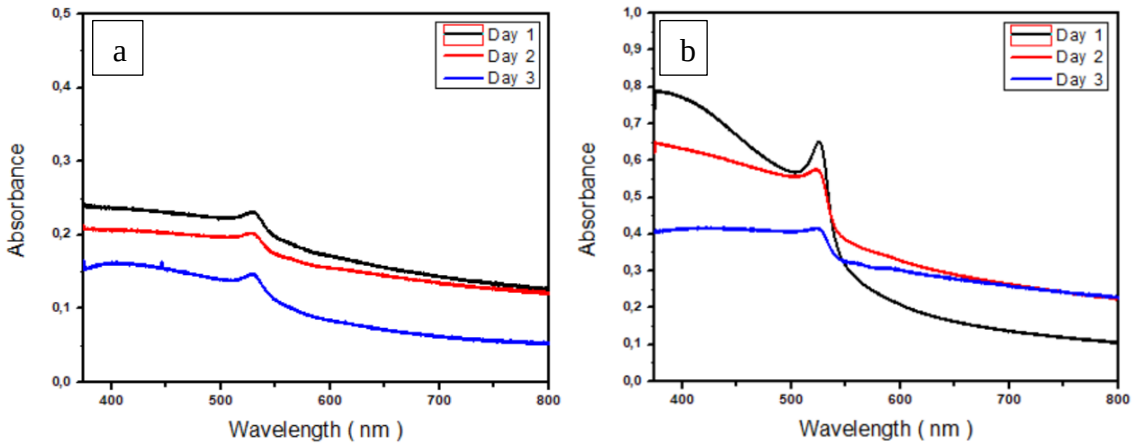

Figure 4.18: UV-Visible spectra of $MAPbBr_3$ a) without and b) with chlorobenzene

4.3. Device Characterization

4.3.1. Current-Voltage Measurements (J-V)

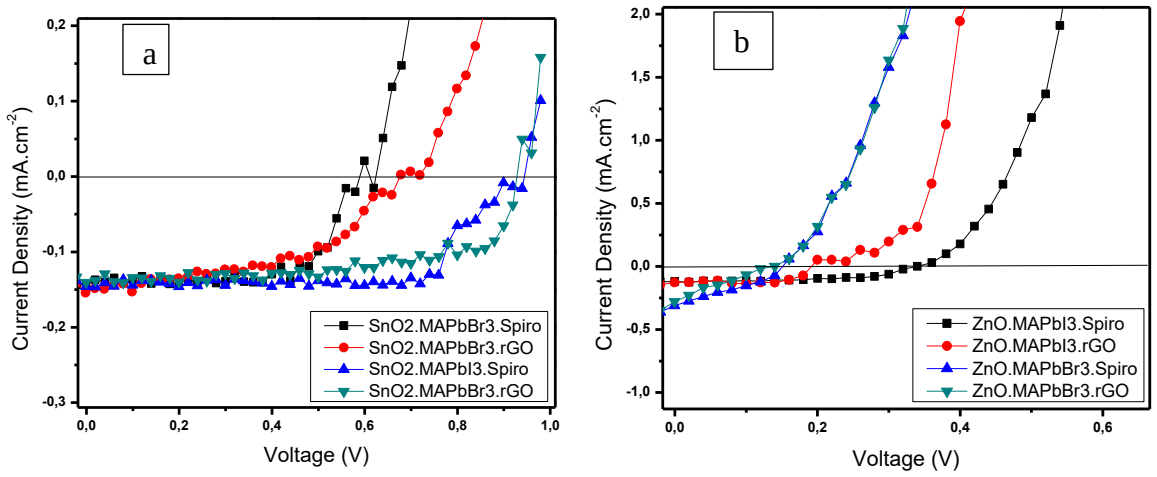

Figure 4.19: The J-V characteristics based on PSCs containing an ETM of a) SnO_2 and b) ZnO under AM 1.5G irradiation (100 $mW.cm^{-2}$)

The performance of the PSC devices was investigated under AM 1.5G irradiation (100 $mW.cm^{-2}$). For this study, a total of eight PSC samples, with a different combination of materials used in the ETL, HTL, and absorbing layer, were fabricated and tested to determine the PSC with the best efficiency. Figure 4.19 above illustrates the J-V curves of the eight PSCs fabricated, with the PSCs using SnO_2 in (a) and ZnO in (b) as an ETM and the corresponding photovoltaic parameters tabulated in table 4.4.

Table 4.4: The photovoltaic parameters of the fabricated PSCs

Samples	V_{OC} (V)	J_{SC} (mA.cm-2)	FF (%)	PCE (%)
SnO_2/$MAPbBr_3$/rGO	0.70	1.47	49.51	0.51
SnO_2/$MAPbBr_3$/Spiro	0.61	1.39	71.80	0.61
SnO_2/$MAPbI_3$/rGO	0.93	1.39	64.16	0.83
SnO_2/$MAPbI_3$/Spiro	0.93	1.42	77.96	1.02
ZnO/$MAPbBr_3$/rGO	0.14	2.99	22.54	0.09
ZnO/$MAPbBr_3$/Spiro	0.15	3.25	30.44	0.15
ZnO/$MAPbI_3$/rGO	0.20	1.35	65.83	0.18
ZnO/$MAPbI_3$/Spiro	0.34	1.23	55.51	0.23

The data displayed in table 4.4 illustrates the correlation between the V_{OC}, $J_{SC,}$ and PCE of the PSCs. The improved current density of SnO_2 can be caused by the reduction of recombination due to improved charge transfer at the SnO_2/Perovskite interface [80]. The PSCs with the highest V_{OC} such as SnO_2/$MAPbI_3$/rGO and SnO_2/$MAPbI_3$/Spiro of 0.93 V displayed the highest PCEs out of the eight samples fabricated with values of 0.83 and 1.02 V, respectively. The PSC ZnO/$MAPbBr_3$/rGO had the lowest FF of 22% and PCE of 0.09 % in comparison to SnO_2/$MAPbI_3$/Spiro**,** which had the highest FF of 77.96% and PCE of 1.02%. The FF of the devices, which is known to determine the quality of a solar cell, ranged from 22 to 77%, with table 4.4 showing that as FF increases, the PCE of the PSC increases. The PSCs employing SnO_2 as an ETM displays PCEs that are approximately four times greater than the PSCs, employing ZnO as the ETM. According to Song *et* al., due to SnO_2 having a lower conduction band energy (CBE) than ZnO, the V_{OC} would be reduced, however, this can be solved using surface passivation. It was discovered that using PbI_2 in the grain boundaries upon annealing could lead to prosperous surface passivation of the $MAPbI_3$ films, leading to the improvement of device performance [75]. As discussed in section 4.1.5.2., SnO_2 displayed the largest time constant of the materials synthesized, indicating that the electron transport would be much faster in comparison to the other materials. The d-spacing calculated from the XRD data showed that SnO_2 had a smaller d-spacing value in comparison to ZnO, resulting in a shorter jumping distance between the particles. Similarly, $MAPbI_3$ has a smaller d-spacing value in comparison to $MAPbBr_3$. Therefore, the PSCs using $MAPbI_3$ and SnO_2, displayed the highest efficiencies in comparison to the other devices.

The low efficiencies obtained for the devices fabricated can be attributed to the degradation of the perovskites back to their lead halide form, which is relatively insulating and has a lower light absorption. The perovskite $MAPbBr_3$ has a lower light absorption and degrades much more rapidly in comparison to its iodide counterpart, therefore, it displays lower efficiencies than the devices employing $MAPbI_3$. The deposition of layers during the fabrication process can be the cause of low performance, as this can be seen in the SEM images presented. The irregularities in the layers, such as non-uniformity and clusters residing on a uniform layer. $MAPbBr_3$ displays greater grain sizes, and consequently greater grain boundaries than that of $MAPbI_3$ as described in section 4.1.1.1 above, which explains the better performance in the cells containing $MAPbI_3$.The deposition process of Ag, the back contact, showed signs of burning on the substrates. These devices were fabricated in the open air with a high relative humidity of approximately 65% without the use of any nitrogen glovebox, this hugely contributed to the fast degradation of the films leading to poor device performances.

CHAPTER FIVE

Conclusion and future work

The following chapter contains a summary of the outcomes obtained in the thesis, concluding the work. Furthermore, recommendations based on possible future work are mentioned based on this study.

5.1. Conclusions

Over the past decade, significant progress has been made to simplify the fabrication of perovskite thin-film solar cells and improve both efficiency and stability of inorganic and inorganic-organic hybrid perovskites. However, poor structure stability that is affected by environmental factors, such as moisture, oxygen, and heat are still hindrances in the large-scale manufacturing process. Therefore, antisolvents, such as chlorobenzene and terephthalic acid, and the doping of perovskites are methods used to increase the performance of the devices.

Research has been done to increase the efficiencies of PSCs, by investigating different materials to be used in the ETL, HTL, and absorbing layer. The PCE of PSCs has reached values as high as 25.5%, however, the stability of the PSCs has still posed a problem.

This project aimed to determine which materials were the most efficient, stable, and cost-effective, by the choice of synthesis, fabrication, and characterization methods used. The materials, $MAPbI_3$, $MAPbBr_3$, SnO_2, ZnO, and rGO, used in this study were fabricated using eight different combinations and tested to determine which combination would produce the most efficient and stable cell. The structural, optical, and electrical properties were investigated using different characterization techniques, namely, HRSEM, XRD, EDS, FTIR, XPS, UV-vis, PL, CV, and EIS.

The hypothesis, that the best combination of materials to produce efficient and stable PSCs using J-V curves, was accepted. Observations indicated that SnO_2 was the best ETM, $MAPbI_3$ the best absorbing layer material, and Spiro-OMeTAD the best HTM. However, with regards to the HTM, the inexpensive alternative, rGO, came significantly close in efficiency. The PSCs using SnO_2 as an ETM, displayed efficiencies approximately four times greater than PSCs using ZnO. The results indicated that the PSC $SnO_2/MAPbI_3$/Spiro displayed the highest efficiency of 1.02 %.

5.2. Recommendations

This project indicated that although the efficiencies were not high, the PSCs worked. The efficiencies can be improved if the stability of the PSC is dealt with. Improvements can be made if the deposition method is improved, resulting in better layer formation, the fabrication takes place in a moisture-free environment, as the moisture degrades the perovskite materials and better attention is paid to the deposition of the metal back contacts, which can burn the materials due to the high temperatures used.

REFERENCES

[1] A. Kojima, K. Teshima, T. Shirai, and T. Miyasaka, "Organometal halide perovskites as visible-light sensitizers for photovoltaic cells," *J. Am. Chem. Soc.*, vol. 131, no. 17, pp. 6050–1, 2009.

[2] A. M. A. Leguy *et al.*, "The dynamics of methylammonium ions in hybrid organic–inorganic perovskite solar cells," *Nat. Commun.*, vol. 6, no. 7124, 2015.

[3] A. Kojima, K. Teshima, Y. Shirai, and T. Miyasaka, "Organometal halide perovskites as visible-light sensitizers for photovoltaic cells," *J. Am. Chem. Soc.*, vol. 131, no. 17, pp. 6050–1, 2009.

[4] H. Chen *et al.*, "An amorphous precursor route to the conformable oriented crystallization of CH3NH3PbBr3 in mesoporous scaffolds: Toward efficient and thermally stable carbon-based perovskite solar cells," *J. Mater. Chem. A*, vol. 4, no. 33, pp. 12897–12912, 2016, doi: 10.1039/c6ta06115j.

[5] H. S. Jung and N. G. Park, "Perovskite solar cells from materials to devices," *Small*, vol. 11, no. 1, pp. 10–25, 2015.

[6] A. K. Chilvery, A. K. Batra, B. Yang, K. Xiao, P. Guggilla, and M. D. Aggarwal, "Perovskites transforming photovoltaics, a mini-review," *J. Phot. Energy*, vol. 5, no. 1, pp. 57402–57402, 2015.

[7] S. Bai *et al.*, "High-performance planar heterojunction perovskite solar cells: Preserving long charge carrier diffusion lengths and interfacial engineering," *Nano Res.*, vol. 7, no. 12, pp. 1749–1758, 2014.

[8] N. Kannan and D. Vakeesan, "Solar energy for future world : - A review," vol. 62, pp. 1092–1105, 2016, doi: 10.1016/j.rser.2016.05.022.

[9] D. Ahuja and M. Tatsutani, "Sustainable energy for developing countries," *Surv. S.A.P.I.E.N.S.*, vol. 2.1, 2009.

[10] S. Jain and P. K. Jain, "The rise of Renewable Energy implementation in South Africa," *Energy Procedia*, vol. 143, no. March, pp. 721–726, 2017, doi: 10.1016/j.egypro.2017.12.752.

[11] S. Panwar, S. Kaushik, and S. Kothari, "Role of renewable energy sources in environmental protection: A review," *Renew Sustain Energy Rev*, vol. 15, no. 3, pp. 1513–1524, 2011.

[12] A. J. Nozik, "Photoelectrochemistry: Applications to solar energy conversion," *Annu. Rev Phys Chem*, vol. 29, no. 1, pp. 189–222, 1978.

[13] B. Schlamadinger *et al.*, "Towards a standard methodology for Greenhouse Gas Balances of Bioenergy Systems in comparison with fossil energy systems," *Biomass and Bioenergy*, vol. 13, no. 6, pp. 359–375, 1997, doi: 10.1016/S0961-9534(97)10032-0.

[14] N. Armaroli and V. Balzani, "The future of energy supply: Challenges and opportunities," *Angew. Chemie Int. Ed.*, vol. 46, no. 1–2, pp. 52–66, 2007.

[15] "Global Horizontal Irradiation (GHI)," *Solar GIS*, 2020. .

[16] E. Fouché and A. Brent, "Journey towards renewable energy for sustainable

development at the local government level: The Case of Hessequa municipality in South Africa," *Sustain.*, vol. 11, no. 3, 2019, doi: 10.3390/su11030755.

[17] M. Chudy, J. Mwaura, D. Walwyn, and J. Lalk, "The Effect of Increased Photovoltaic Energy Generation on Electricity Price and Capacity in South Africa," 2015.

[18] M. C. Mathpal, P. Kumar, F. H. Aragón, M. A. G. Soler, and H. C. Swart, *Basic Concepts, Engineering, and Advances in Dye-Sensitized Solar Cells*. 2020.

[19] K. W. J. Barnham, M. Mazzer, B. Clive, J. Wiley, and S. Limited, "Resolving the energy crisis : nuclear or photovoltaics ?," vol. 5, no. March, pp. 161–164, 2006.

[20] V. T. Chebrolu and H. J. Kim, "Recent progress in quantum dot sensitized solar cells: An inclusive review of photoanode, sensitizer, electrolyte, and the counter electrode," *J. Mater. Chem. C*, vol. 7, no. 17, pp. 4911–4933, 2019, doi: 10.1039/c8tc06476h.

[21] T. Benanti, "Organic Solar Cells." NACK Network, 2018, [Online]. Available: https://nanohub.org/resources/27835.

[22] M. B. Hayat, D. Ali, K. C. Monyake, L. Alagha, and N. Ahmed, "Solar energy—A look into power generation, challenges, and a solar-powered future," *Int. J. Energy Res.*, vol. 43, no. 3, pp. 1049–1067, 2019, doi: 10.1002/er.4252.

[23] S. A. Olaleru, J. K. Kirui, D. Wamwangi, K. T. Roro, and B. Mwakikunga, "Perovskite solar cells: The new epoch in photovoltaics," *Sol. Energy*, vol. 196, no. December 2019, pp. 295–309, 2020, doi: 10.1016/j.solener.2019.12.025.

[24] A. M. Bagher, M. M. A. Vahid, and M. Mohsen, "Types of Solar Cells and Application," *Am. J. Opt. Photonics*, vol. 3, no. 5, pp. 94–113, 2015.

[25] M. Krebs-Moberg, M. Pitz, T. L. Dorsette, and S. H. Gheewala, "Third generation of photovoltaic panels: A life cycle assessment," *Renew. Energy*, vol. 164, pp. 556–565, 2021, doi: 10.1016/j.renene.2020.09.054.

[26] W. Soutter, "Nanotechnology in Solar Power," *AZoNano*, 2020, Accessed: Mar. 18, 2022. [Online]. Available: https://www.azonano.com/article.aspx?ArticleID=3068.

[27] S. Almosni *et al.*, "Material challenges for solar cells in the twenty-first century: directions in emerging technologies," *Sci. Technol. Adv. Mater.*, vol. 19, no. 1, pp. 336–369, 2018, doi: 10.1080/14686996.2018.1433439.

[28] S. Sharma, K. K. Jain, and A. Sharma, "Solar Cells: In Research and Applications—A Review," *Mater. Sci. Appl.*, vol. 06, no. 12, pp. 1145–1155, 2015, doi: 10.4236/msa.2015.612113.

[29] M. E. Ragoussi and T. Torres, "New generation solar cells: Concepts, trends and perspectives," *Chem. Commun.*, vol. 51, no. 19, pp. 3957–3972, 2015, doi: 10.1039/c4cc09888a.

[30] Y. Chen, L. Zhang, Y. Zhang, H. Gao, and H. Yan, "Large-area perovskite solar cells - a review of recent progress and issues," *R. Soc. Chem. Adv.*, vol. 8, no. 10489, 2018, doi: 10.1039/cBra00384.

[31] L. Mcgovern, M. H. Futscher, L. A. Muscarella, and B. Ehrler, "Understanding the Stability of MAPbBr 3 versus MAPbI 3 : Suppression of Methylammonium Migration and Reduction of Halide Migration," 2020, doi: 10.1021/acs.jpclett.0c01822.

[32] K. Domanski, “The Quest for Stability of Perovskite Solar Cells : Understanding Degradation , Improving Lifetimes PAR,” vol. 8106, 2018.

[33] I. Van De Riet, H. Fang, S. Adjokatse, S. Kahmann, and M. A. Loi, “Influence of morphology on photoluminescence properties of methylammonium lead tribromide films,” *J. Lumin.*, vol. 220, p. 117033, 2020, doi: 10.1016/j.jlumin.2020.117033.

[34] K. Wu *et al.*, “High Efficiency and Robust Performance of Organo Lead Perovskite Solar Cells with Large Grain Absorbers Prepared in Ambient Air Conditions High Efficiency and Robust Performance of Organo Lead Perovskite Solar Cells with Large Grain Absorbers Prepared in ,” 2014, doi: 10.1246/cl.140919.

[35] C. S. Shim and C. K. Hong, “Highly stable and efficient solid-state solar cells based on methylammonium lead bromide (CH3NH3PbBr3) perovskite quantum dots,” vol. 7, no. 8, pp. e208-9, 2015, doi: 10.1038/am.2015.86.

[36] J. Stenberg, “Perovskite solar cells,” 2017.

[37] A. Marchioro *et al.*, “Unravelling the mechanism of photoinduced charge transfer processes in lead iodide perovskite solar cells,” *Nat. Photonics*, vol. 8, no. 3, pp. 250–255, 2014, doi: 10.1038/nphoton.2013.374.

[38] X. Hou, S. Huang, W. Ou-yang, L. Pan, Z. Sun, and X. Chen, “Constructing Efficient and Stable Perovskite Solar Cells via Interconnecting Perovskite Grains,” 2017, doi: 10.1021/acsami.7b08488.

[39] C. Aranda, A. Guerrero, and J. Bisquert, “Ionic Effect Enhances Light Emission and the Photovoltage of Methylammonium Lead Bromide Perovskite Solar Cells by Reduced Surface Recombination,” *ACS Energy Lett.*, vol. 4, pp. 741–746, 2019, doi: 10.1021/acsenergylett.9b00186.

[40] Y. Vaynzof, “The Future of Perovskite Photovoltaics—Thermal Evaporation or Solution Processing?,” *Adv. Energy Mater.*, vol. 10, no. 48, 2020, doi: 10.1002/aenm.202003073.

[41] M. Petrović, V. Chellappan, and S. Ramakrishna, “Perovskites: Solar cells & engineering applications - materials and device developments,” *Sol. Energy*, vol. 122, pp. 678–699, 2015, doi: 10.1016/j.solener.2015.09.041.

[42] A. Chilvery, S. Das, P. Guggilla, C. Brantley, and A. Sunda-Meya, “A perspective on the recent progress in solution-processed methods for highly efficient perovskite solar cells,” *Sci. Technol. Adv. Mater.*, vol. 17, no. 1, pp. 650–658, 2016, doi: 10.1080/14686996.2016.1226120.

[43] N. K. Elumalai, M. A. Mahmud, D. Wang, and A. Uddin, “Perovskite Solar Cells: Progress and Advancements,” *Energies*, vol. 9, no. 11, p. 861, 2016, doi: https://doi.org/10.3390/en9110861.

[44] M. Habibi, F. Zabihi, M. R. Ahmadian-Yazdi, and M. Eslamian, “Progress in emerging solution-processed thin film solar cells - Part II: Perovskite solar cells,” *Renew. Sustain. Energy Rev.*, vol. 62, pp. 1012–1031, 2016, doi: 10.1016/j.rser.2016.05.042.

[45] I. A. Howard *et al.*, “Coated and Printed Perovskites for Photovoltaic Applications,” *Adv. Mater.*, vol. 31, no. 26, 2019, doi: 10.1002/adma.201806702.

[46] A. T. Barrows, A. J. Pearson, C. K. Kwak, A. D. F. Dunbar, A. R. Buckley, and D. G. Lidzey, "Efficient planar heterojunction mixed-halide perovskite solar cells deposited via spray-deposition," *Energy Environ. Sci.*, no. 7, pp. 2944–2950, 2014.

[47] J. Kim *et al.*, "Overcoming the challenges of large-area high-efficiency perovskite solar cells," *ACS Energy Lett.*, no. 2, pp. 1978–1984, 2017.

[48] X. Dai, K. Xu, and F. Wei, "Recent progress in perovskite solar cells: the perovskite layer," *Beilstein J. Nanotechnol.*, vol. 11, pp. 51–60, 2020, doi: 10.3762/bjnano.11.5.

[49] L. A. Frolova *et al.*, "Highly efficient all-inorganic planar heterojunction perovskite solar cells produced by thermal coevaporation of CsI and PbI2," *J. Phys. Chem. Lett.*, no. 8, pp. 67–72, 2017.

[50] M. Khazaee *et al.*, "A versatile thin-film deposition method for multidimensional semiconducting bismuth halides," *Chem. Mater.*, no. 30, pp. 3538–3544, 2018.

[51] Y. Kyosuke *et al.*, "Annealing effects on CsPbI3-based planar heterojunction perovskite solar cells formed by vacuum deposition method," *Jpn. J. Appl. Phys.*, vol. 56, no. 04CS11, 2017.

[52] M. Shahiduzzaman *et al.*, "Improved Reproducibility and intercalation control of efficient planar inorganic perovskite solar cells by simple alternate vacuum deposition of PbI2 and CsI," *ACS Omega*, no. 2, pp. 4464–4469, 2017.

[53] M. Shariati and G. Vahid, "The annealing investigation on morphology and photoluminescence properties of In2O3 1-D nanostructures in resistive evaporation mechanism," *Eur. Phys. J. Appl. Phys.*, vol. 65, no. 2, 2014.

[54] J. Ávila, C. Momblona, P. P. Boix, M. Sessolo, and H. J. Bolink, "Vapor-Deposited Perovskites: The Route to High-Performance Solar Cell Production?," *Joule*, vol. 1, no. 3, pp. 431–442, 2017, doi: 10.1016/j.joule.2017.07.014.

[55] Y. H. Chiang, M. Anaya, and S. D. Stranks, "Multisource Vacuum Deposition of Methylammonium-Free Perovskite Solar Cells," *ACS Energy Lett.*, vol. 5, no. 8, pp. 2498–2504, 2020, doi: 10.1021/acsenergylett.0c00839.

[56] M. Sessolo, C. Momblona, L. Gil-Escrig, and H. J. Bolink, "Photovoltaic devices employing vacuum-deposited perovskite layers," *MRS Bull.*, vol. 40, no. 8, pp. 660–666, 2015, doi: 10.1557/mrs.2015.170.

[57] A. M. Igual-Muñoz, J. Navarro-Alapont, C. Dreessen, F. Palazon, M. Sessolo, and H. J. Bolink, "Room-Temperature Vacuum Deposition of CsPbI2Br Perovskite Films from Multiple Sources and Mixed Halide Precursors," *Chem. Mater.*, vol. 32, no. 19, pp. 8641–8652, 2020, doi: 10.1021/acs.chemmater.0c03038.

[58] A. Babaei, W. Soltanpoor, M. A. Tesa-Serrate, S. Yerci, M. Sessolo, and H. J. Bolink, "Preparation and Characterization of Mixed Halide MAPbI3−xClx Perovskite Thin Films by Three-Source Vacuum Deposition," *Energy Technol.*, vol. 8, no. 4, pp. 1–5, 2020, doi: 10.1002/ente.201900784.

[59] X. Huang, H. Guo, J. Yang, K. Wang, X. Niu, and X. Liu, "Moderately reduced graphene oxide / PEDOT : PSS as hole transport layer to fabricate ef fi cient perovskite hybrid solar cells," *Org. Electron.*, vol. 39, pp. 288–295, 2016, doi: 10.1016/j.orgel.2016.10.013.

[60] C. Liu, Y. Xu, and Y. Y. Noh, “Contact engineering in organic field-effect transistors,” *Mater. Today*, vol. 18, pp. 79–96, 2015.

[61] B. Lussem, C. M. Keum, D. Kasemann, B. Naab, Z. Bao, and K. Leo, “Doped Organic Transistors,” *Chem. Rev.*, vol. 116, pp. 13714–13751, 2016.

[62] P. Gao, R. Scopelliti, E. Mosconi, M. Graetzel, and M. K. Nazeeruddin, “A molecularly engineered hole-transporting material for efficient perovskite solar cells,” vol. 1, no. February, pp. 1–7, 2016, doi: 10.1038/NENERGY.2015.17.

[63] J. Urieta-Mora, I. García-Benito, A. Molina-Ontoria, and N. Martín, “Hole transporting materials for perovskite solar cells: a chemical approach,” *Chem. Soc. Rev.*, vol. 47, no. 23, pp. 8541–8571, 2018, doi: 10.1039/c8cs00262b.

[64] N. J. Jeon *et al.*, “A fluorene-terminated hole-transporting material for highly efficient and stable perovskite solar cells,” *Nat. Energy*, vol. 3, no. August, 2018, doi: 10.1038/s41560-018-0200-6.

[65] A. L. Palma *et al.*, “Author ’ s Accepted Manuscript Reduced Graphene Oxide as Efficient and Stable Hole Transporting Material in Mesoscopic Perovskite Solar Cells,” *Nano Energy*, 2016, doi: 10.1016/j.nanoen.2016.02.027.

[66] A. A. Babaev *et al.*, “Functionalized rGO interlayers improve the fill factor and current density in PbS QDs-based solar cells,” *Materials (Basel).*, vol. 12, no. 24, 2019, doi: 10.3390/MA12244221.

[67] M. Singh, A. Yadav, S. Kumar, and P. Agarwal, “Annealing induced electrical conduction and band gap variation in thermally reduced graphene oxide films with different sp 2 /sp 3 fraction,” *Appl. Surf. Sci.*, vol. 326, pp. 236–242, 2015, doi: 10.1016/j.apsusc.2014.11.121.

[68] S. Z. Haider, H. Anwar, Y. Jamil, and M. Shahid, “A comparative study of interface engineering with different hole transport materials for high-performance perovskite solar cells,” *J. Phys. Chem. Solids*, vol. 136, no. July 2019, p. 109147, 2020, doi: 10.1016/j.jpcs.2019.109147.

[69] H. Kim *et al.*, “Article Reduced Graphene Oxide Improves Moisture and Thermal Stability of Perovskite Solar Cells Reduced Graphene Oxide Improves Moisture and Thermal Stability of Perovskite Solar Cells,” 2020, doi: 10.1016/j.xcrp.2020.100053.

[70] H. Feng, R. Cheng, X. Zhao, X. Duan, and J. Li, “A low-temperature method to produce highly reduced graphene oxide,” *Nat. Commun.*, vol. 4, pp. 1537–1539, 2013, doi: 10.1038/ncomms2555.

[71] H. Xie *et al.*, “Solvothermal synthesis of highly crystalline SnO2 nanoparticles for flexible perovskite solar cells application,” *Mater. Lett.*, 2018, doi: 10.1016/j.matlet.2018.09.117.

[72] A. Aboulouard, B. Gultekin, M. Can, and M. Erol, “Dye sensitized solar cells based on titanium dioxide nanoparticles synthesized by flame spray pyrolysis and hydrothermal sol-gel methods : a comparative study on photovoltaic performances,” *Integr. Med. Res.*, no. x x, pp. 1–9, 2019, doi: 10.1016/j.jmrt.2019.11.083.

[73] Z. H. Wang, “Low-temperature processed SnO2 compact layer for efficient mesostructure perovskite solar cells,” *Appl. Surf. Sci.*, 2016, doi: 10.1016/j.apsusc.2016.06.187.

[74] H. Rao, B. Chen, W. Li, Y. Xu, and H. Chen, “Improving the Extraction of Photogenerated Electrons with SnO 2 Nanocolloids for Effi cient Planar Perovskite Solar Cells,” pp. 7200–7207, 2015, doi: 10.1002/adfm.201501264.

[75] J. Song *et al.*, “Low-temperature SnO2-based electron selective contact for efficient and stable perovskite solar cells,” *J. Mater. Chem. A*, vol. 3, no. 20, pp. 10837–10844, 2015, doi: 10.1039/c5ta01207d.

[76] P. Shen, C. Tseng, T. Kuo, C. Shih, and M. Li, “ScienceDirect Microwave-assisted synthesis of titanium dioxide nanocrystalline for efficient dye-sensitized and perovskite solar cells,” *Sol. ENERGY*, vol. 120, pp. 345–356, 2015, doi: 10.1016/j.solener.2015.07.036.

[77] Y. Xiao, G. Han, Y. Chang, Y. Zhang, Y. Li, and M. Li, “Investigation of perovskite-sensitized nanoporous titanium dioxide photoanodes with different thicknesses in perovskite solar cells,” *J. Power Sources*, vol. 286, pp. 118–123, 2015, doi: 10.1016/j.jpowsour.2015.03.152.

[78] W. Zhao, H. Li, D. Li, Z. Liu, D. Wang, and S. F. Liu, “Comprehensive investigation of sputtered and spin-coated zinc oxide electron transport layers for highly efficient and stable planar perovskite solar cells,” *J. Power Sources*, vol. 427, no. April, pp. 223–230, 2019, doi: 10.1016/j.jpowsour.2019.04.088.

[79] Y. Cheng, Q. Yang, J. Xiao, and Q. Xue, “On the Decomposition of Organometal Halide Perovskite Films on Zinc Oxide Nanoparticles On the Decomposition of Organometal Halide Perovskite Films on Zinc Oxide Nanoparticles,” *Appl. Mater. Interfaces*, 2015, doi: 10.1021/acsami.5b04695.

[80] Y. Sun *et al.*, “Journal of Solid State Chemistry Comparison of effects of ZnO and TiO 2 compact layer on performance of perovskite solar cells,” *J. Solid State Chem.*, vol. 287, no. April, p. 121387, 2020, doi: 10.1016/j.jssc.2020.121387.

[81] D. Liu and T. L. Kelly, “solution processing techniques,” *Nat. Photonics*, vol. 8, no. 2, pp. 133–138, 2013, doi: 10.1038/nphoton.2013.342.

[82] C. M. Pelicano and H. Yanagi, “Efficient Solid-State Perovskite Solar Cells BAsed on Nanostructured Zinc Oxide Designed by Strategic Low Temperature Water Oxidation,” *J. Mater. C*, 2017, doi: 10.1039/C7TC01934C.

[83] L. Chen *et al.*, “Low-temperature synthesis of tin dioxide hollow nanospheres and their potential applications in dye-sensitized solar cells and photoelectrochemical type self-powered ultraviolet photodetectors,” *J. Power Sources*, vol. 272, pp. 886–894, 2014, doi: 10.1016/j.jpowsour.2014.09.021.

[84] H. Benhebal, B. Benrabah, A. E. K. Ammari, and Y. Madoune, “STRUCTURAL AND OPTOELECTRONIC PROPERTIES OF SnO 2 THIN FILMS DOPED BY GROUP-IA ELEMENTS,” vol. 25, no. 2, pp. 1–6, 2018, doi: 10.1142/S0218625X18500075.

[85] T. Matsui, W. Tress, M. Saliba, A. Abate, M. Gra, and A. Hagfeldt, “Environmental Science cells by solution-processed tin oxide †,” *Energy Environ. Sci.*, 2016, doi: 10.1039/C6EE02390H.

[86] Z. Li *et al.*, “One-Pot Synthesis of Mesoporous TiO 2 Micropheres and Its Application for High-E ffi ciency Dye-Sensitized Solar Cells,” 2015, doi:

10.1021/acsami.5b02195.

[87] D. Shen *et al.*, "Understanding the solvent-assisted crystallization mechanism inherent in e ffi cient organic – inorganic halide perovskite solar cells †," *J. Mater. Chem. A Mater. energy Sustain.*, vol. 2, pp. 20454–20461, 2014, doi: 10.1039/C4TA05635C.

[88] R. Petersen, "Evaluation of CuSCN as a Hole Transport Layer in Flexible Perovskite Solar Cells."

[89] A. Mhamdi, H. Mehdi, and A. Bouazizi, "Effect of solvents and annealing treatment on the properties of the methylammonium lead tribromide perovskite thin films," *J. Mater. Sci. Mater. Electron.*, vol. 32, no. 2, pp. 2302–2311, 2021, doi: 10.1007/s10854-020-04994-0.

[90] M. M. Stylianakis *et al.*, "Updating the Role of Reduced Graphene Oxide Ink on Field Emission Devices in Synergy with Charge Transfer Materials," *Nanomaterials*, vol. 9, no. 137, pp. 1–15, 2019, doi: 10.3390/nano9020137.

[91] D. Li, J. Cui, H. Li, D. Huang, M. Wang, and Y. Shen, "ScienceDirect Graphene oxide modified hole transport layer for CH 3 NH 3 PbI 3 planar heterojunction solar cells," vol. 131, pp. 176–182, 2016.

[92] M. A. Basyooni, Y. Ramazan, and M. Yilmaz, "Superlattices and Microstructures Structural , optical , electrical and room temperature gas sensing characterizations of spin coated multilayer cobalt-doped tin oxide thin films," *Superlattices Microstruct.*, vol. 140, no. x, p. 106465, 2020, doi: 10.1016/j.spmi.2020.106465.

[93] Q. Dong *et al.*, "Insight into Perovskite Solar Cells Based on SnO Compact Electron-Selective Layer Insight into Perovskite Solar Cells Based on SnO 2 Compact Electron-Selective Layer," 2015, doi: 10.1021/acs.jpcc.5b00541.

[94] P. Solar, C. A. Review, and F. Sani, "Advancement on Lead-Free Organic-Inorganic Halide," pp. 1–17, doi: 10.3390/ma11061008.

[95] M. R. Ahmadian-Yazdi, F. Zabihi, M. Habibi, and M. Eslamian, "Effects of Process Parameters on the Characteristics of Mixed-Halide Perovskite Solar Cells Fabricated by One-Step and Two-Step Sequential Coating," *Nanoscale Res. Lett.*, vol. 11, no. 1, 2016, doi: 10.1186/s11671-016-1601-8.

[96] M. Sulaman, S. Yang, Y. Jiang, Y. Tang, and B. Zou, "Enhanced performance of solution-processed broadband photodiodes by epitaxially blending MAPbBr3 quantum dots and ternary PbSxSe1-x quantum dots as the active layer," *Nanotechnology*, pp. 0–30, 2017.

[97] A. Nur'aini, S. Lee, and I. Oh, "Ion Migration in Metal Halide Perovskite," *J. Electrochem. Sci. Technol.*, vol. 13, no. 1, pp. 71–77, 2022.

[98] X. Guan *et al.*, "Light-Responsive Ion-Redistribution-Induced Resistive Switching in Hybrid Perovskite Schottky Junctions," *Adv. Funct. Mater.*, vol. 28, 2018.

[99] J. Cao *et al.*, "Communication Material for Efficient and Stable Perovskite Solar Cells Well-Defined Thiolated Nanographene as Hole-Transporting Material for Efficient and Stable Perovskite Solar Cells," 2015, doi: 10.1021/jacs.5b06493.

[100] M. I. Ahmed, Z. Hussain, M. Mujahid, A. N. Khan, S. S. Javaid, and A. Habib, "Low resistivity ZnO-GO electron transport layer based CH3NH3PbI3 solar cells," *AIP Adv.*,

vol. 6, no. 6, 2016, doi: 10.1063/1.4953397.

[101] C. G. Kumar, S. Pombala, Y. Poornachandra, and S. V. Agarwal, *Nanobiomaterials in Antimicrobial Therapy*, Applicatio. William Andrew: Applied Science Publishers, 2016.

[102] A. M. Ali *et al.*, "Morphological and Optical Properties of SnO2 Doped ZnO Nanocomposites for Electrochemical Sensing of Hydrazine," *Int. J. Electrochem. Sci.*, vol. 14, pp. 1461–1478, 2019.

[103] W. Rittisut, "Synthesis and Characterizationof Methylammonium Lead Iodide Bromide Perovskites," Suranaree University of Technology, 2017.

[104] A. F. Akbulatov *et al.*, "Light or Heat: What is Killing Lead Halide Perovskites under Solar Cell Operation Conditions?," *J. Phys. Chem. Lett.*, vol. 11, pp. 333–339, 2020.

[105] D. W. Boukhvalov *et al.*, "Thermal Effects and Halide Mixing of Hybrid Perovskites: MD and XPS Studies," *J. Phys. Chem. A*, vol. 124, pp. 135–140, 2020.

[106] A. G. Boldyreva *et al.*, "Unravelling the Material Composition Effects on the Gamma Ray Stability of Lead Halide Perovskite Solar Cells: MAPbI3 Breaks the Records," *J. Phys. Chem. Lett.*, vol. 11, pp. 2630–2636, 2020.

[107] C. Wang, B. R. Ecker, H. Wei, J. Huang, and Y. Gao, "Environmental Surface Sttability of the MAPbBr3 Single Crystal," *J. Phys. Chem. C*, vol. 122, pp. 3513–3522, 2018.

[108] F. A. Akgul *et al.*, "Structural and electronic properties of SnO2," *J. Alloys Compd.*, vol. 579, pp. 50–56, 2013.

[109] A. Saaedi *et al.*, "XPS studies and photocurrent applications of alkali-metals-doped ZnO nanoparticles under visible illumination conditions," *Phys. E*, vol. 79, pp. 113–118, 2016.

[110] M. Chen *et al.*, "X-ray phoyoelectron spectroscopy and auger electron spectroscopy studies of Al-doped ZnO films," *Appl. Surf. Sci.*, vol. 158, no. 1–2, pp. 134–140, 2000.

[111] J. C. C. Fan and J. B. Goodenough, "X-Ray Photoemission Spectroscopy Studies of Sn-Doped Indium-Oxide Films," *J. Appl. Phys.*, vol. 4B, pp. 3524–3531, 1977.

[112] J. Das *et al.*, "Micro-Raman and XPS studies of pure ZnO ceramics," *Phys. B*, vol. 405, pp. 2492–2497, 2010.

[113] H. Feng, R. Cheng, X. Zhao, X. Duan, and J. Li, "A low-temperature method to produce highly reduced graphene oxide," *Nat. Commun.*, vol. 4, pp. 1537–1539, 2013, doi: 10.1038/ncomms2555.

[114] M. Marikkannan and J. M. Pearce, "Digital Commons @ Michigan Tech A Novel Synthesis of Tin Oxide Thin Films by the Sol-gel Process for Optoelectronic Applications," 2015, doi: 10.1063/1.4909542.

[115] Y. Shen *et al.*, "Evolution of the band-gap and optical properties of graphene oxide with controllable reduction level," *Carbon N. Y.*, vol. 62, pp. 157–164, 2013.

[116] A. S. Shatla, P. P. Bawol, and H. Baltruschat, "Adsorption of Iodide and Bromide on Au(111) Electrodes from Aprotic Electrolytes: Role of the Solvent," *ChemElectroChem*, vol. 7, pp. 4782–4793, 2020.

[117] X. Liu, C. Xu, and E. Lee, “Chlorobenzene-Mediated Control of Crystallization in Perovskite Films for High-Performance Solar Cells,” 2020, doi: 10.1021/acsaem.0c02342.